ARCHIVES OF MECHANICS
Arch. Mech. **73** (5–6), 499–540, 2021, DOI: 10.24423/aom.3813

Application of a geometrically nonlinear elastoplastic gradient-enhanced damage model with incremental potential to composite microstructures

H. BOUSSETTA, J. DITTMANN, S. WULFINGHOFF

Institute for Materials Science, Faculty of Engineering, Kiel University Kaiserstr. 2, 24143 Kiel, Germany, e-mails: hajer.bossetta91@gmail.com, swu@tf.uni-kiel.de, jd@tf.uni-kiel.de

The prediction of inelastic processes like plastic deformations and cracks within the microstructure of modern man-made materials by realistic, yet simple and efficient continuum models remains a major task in material modelling. For this purpose, gradient-extended standard dissipative solids represent one of the most promising model classes, which is also formulated and applied in this work to investigate microscopic failure mechanisms in three exemplary three-dimensional composite microstructures. The model combines geometrically nonlinear isotropic elastoplasticity with an isotropic damage model with gradient-extension. For the numerical treatment, a variational constitutive update algorithm based on the exponential map is applied. The model is used to provide insight into the microscopic failure of a brittle woven composite material, a particle-reinforced plastic and a carbon fiber reinforced composite. The influence of different microstructural and material parameters on the overall failure behavior is characterized. Adaptive meshing is used to enable a refined numerical resolution of the cracked regions.

Key words: damage, plasticity, cracks, composites, toughening.

1. Introduction

While structural applications of composite materials are increasing in several engineering fields where high stiffness and strength-to-weight ratios and long fatigue life are required, there is always room for optimization to ensure optimum performance especially when severe operational constraints are imposed, therefore composite structures are usually tailored, depending on specific objectives. In particular, the enhancement of the mechanical properties of novel composite materials has always been of high interest for designers with a special focus on properties relevant to strength and service life to meet requirements imposed by the industrial application involved. Indeed, aware that the behavior of the composite materials is significantly influenced by the underlying microstructure, this work aims to investigate this effect numerically which could allow for a combination between the material microstructural parameters

in order to obtain an optimized composite material in terms of performance. Admittedly, experimental investigations could provide a clear overview of the effect of the microstructural parameters on the mechanical properties. However, quantifying this effect experimentally and finding the best combination between parameters leading to the best performance would be extremely expensive in terms of money, time, and effort. And here manifests itself the requirement of the development of a computational tool in order to carry out such investigations which is the aim of the present work. To reach this goal, a campaign of numerical tests has been conducted through a micro-scale numerical study aiming to a quick and cost-effective prediction of the overall mechanical properties of three exemplary composite materials with different microstructures. Indeed, a geometrically nonlinear elastoplastic gradient-enhanced damage model with incremental potential has been applied to (a) woven glass fiber/epoxy composite, (b) core-shell ruber (CSR) particles/epoxy composite, and (c) unidirectional carbon fiber/epoxy composite.

The prediction of inelastic processes like plastic deformations and cracks within the micro-structure of novel composite materials by realistic, yet simple and efficient continuum models remains a major task in material modeling. We cite in the following overview an (incomplete) list of the most competitive models developed and applied for this purpose. Indeed, phenomenological models of geometrically nonlinear elastoplasticity nowadays mostly build on the concept of internal variables [1] and the multiplicative decomposition of the deformation gradient into elastic and plastic parts [2, 3]. An additional decomposition of the plastic part yields a conceptually sound basis for kinematic hardening [4, 5]. Often, the plastic deformation is assumed to be incompressible, which poses special challenges on the numerical treatment, but can exactly be described using, e.g., time integration algorithms based on the exponential map [6–8, and many more]. This approach is naturally (but not necessarily) accompanied by logarithmic (Hencky) strain measures. Many of the aforementioned models fall into the class of generalized standard materials [9], where a dissipation potential defines the dissipative processes and the constitutive evolution equations (see also [10]). If the dissipation potential meets certain conditions, the material model is automatically guaranteed to obey the second law of thermo- dynamics. Such models have not only been used to model material behavior on the structural level but also enabled important developments in the field of microscopic material modelling, e.g., in the context of homogenization of elastoplastic microstructures (for an overview see [11]). An important milestone in this regard were so-called 'variational constitutive updates', i.e., the generalization of incremental potentials to the algorithmic context in the sense that the time-discrete model is based on a potential, which is consistent with its time continuous counterpart in the limit case of infinitesimal time steps [12]. Amongst other things, the potential-based structure has the ad-

vantage that it does not only open new doors for time discretization schemes but also for mathematical analysis (e.g., [13]) and microstructure evolution modelling (e.g., [14, 15]). Besides plastic deformations, continuum damage mechanics, as a second major topic in the field of inelastic deformations, has grown to an important field in material modelling since the pioneering work of Kachanov [16]. Phenomenological internal variables, describing damage on a structural scale, include scalars ([17–19] amongst many others), vectors (e.g., [20]) or tensors of various order (e.g., [21, 22]), which bears the risk of hidden conceptual problems and unphysical behavior (see, e.g. [23, 24]). At some point of the deformation process, damage usually leads to localization effects, indicating the onset of a macroscopic crack. Damage models without internal length scale then lead to an artificially vanishing dissipation (if the mesh is continuously refined). Therefore, nonlocal models (e.g., [25]) have been proposed and were further developed towards gradient-extended models like implicit gradient models [26]. More recent works in many cases introduce generalized stresses and tractions work-conjugate to the inelastic variable and its gradient in the sense of Gurtin [27, 28], a concept being also extensively used in gradient plasticity for the modelling of size effects (e.g., [29–32]). Phase field models of fracture are closely related to that [33–37], which however originated from the idea of regularizing a Griffith-like energy functional [38] and had a tremendous impact on countless subsequent publications. Generalizations towards elastoplasticity can be found in, e.g., [39–41]. A formal framework for gradient-extended standard dissipative solids has been formulated in [42]. Based on all these models and studies, a geometrically nonlinear isotropic elasto-plastic model and an isotropic gradient-extended damage model have been developed and combined to characterize the non-linear elastoplastic behavior of particle-reinforced plastics and fiber-reinforced plastics as well as to investigate the microscopic failure in these complex composite micro-structures. In this work, a geometrically nonlinear gradient-extended isotropic damage-plasticity model is considered, which combines various model ingredients from the literature. The performance of the model is then used to investigate three exemplary composite types (woven composite, particle- and fiber-reinforced) and the influence of various microstructural features as well as the material properties on the overall composite performance. The study is purely theoretical. A detailed comparison with experimental results remains a task for the future.

2. Model formulation

2.1. Kinematics

The model makes use of the multiplicative decomposition of the deformation gradient $\mathbf{F}$ into elastic and plastic parts $\mathbf{F}^{\mathrm{e}}$ and $\mathbf{F}^{\mathrm{p}}$ [2, 3], and the polar decom-

position into a proper orthorgonal rotation tensor $\mathbf{R}$ and the positive definite right and left stretch tensors $\mathbf{U}$ and $\mathbf{V}$:

$$\mathbf{F} = \mathrm{Grad}(\mathbf{x}(\mathbf{X}, t)) = \mathbf{F}^{\mathrm{e}}\mathbf{F}^{\mathrm{p}} = \mathbf{R}\mathbf{U} = \mathbf{V}\mathbf{R}. \tag{2.1}$$

Here, $\mathbf{x}$ and $\mathbf{X}$ denote the position vectors in the current configuration V and initial configuration V_0, respectively. The right plastic Cauchy–Green tensor $\mathbf{C}^{\mathrm{p}}$, left elastic Cauchy–Green tensor $\mathbf{b}^{\mathrm{e}}$ and the elastic Hencky strain ε^{e} are given by

$$\mathbf{C}^{\mathrm{p}} = \mathbf{F}^{\mathrm{p}\top}\mathbf{F}^{\mathrm{p}}, \quad \mathbf{b}^{\mathrm{e}} = \mathbf{F}^{\mathrm{e}}\mathbf{F}^{\mathrm{e}\top}, \quad \varepsilon^{\mathrm{e}} = \frac{1}{2}\ln \mathbf{b}^{\mathrm{e}}. \tag{2.2}$$

Furthermore, the plastic velocity 'gradient' $\mathbf{L}^{\mathrm{p}}$ and its symmetric part $\mathbf{D}^{\mathrm{p}}$ read

$$\mathbf{L}^{\mathrm{p}} = \dot{\mathbf{F}}^{\mathrm{p}}\mathbf{F}^{\mathrm{p}-1}, \qquad \mathbf{D}^{\mathrm{p}} = \mathrm{sym}(\mathbf{L}^{\mathrm{p}}) = \frac{1}{2}\mathbf{F}^{\mathrm{p}\top}\dot{\mathbf{C}}^{\mathrm{p}}\mathbf{F}^{\mathrm{p}}. \tag{2.3}$$

Plastic incompressibility is enforced by the constraint

$$\det \mathbf{F}^{\mathrm{p}} = 1, \tag{2.4}$$

which can be shown to be equivalent to the requirement $\mathrm{tr}(\mathbf{D}^{\mathrm{p}}) = 0$.

2.2. Free energy and dissipation potential

The free energy ψ is assumed to take the following form (compare, e.g., [39–41]):

$$\psi = g(D)\big(\psi_{\mathrm{e}+}(\varepsilon^{\mathrm{e}}) + \beta\sigma_{\mathrm{y}0}\alpha + \psi_{\mathrm{p}}(\alpha)\big) + \psi_{\mathrm{e}-}(\varepsilon^{\mathrm{e}}) + \frac{1}{2}g_{\mathrm{c}}^{\mathrm{e}}\left(\frac{D^2}{l} + l\|\mathrm{Grad}(D)\|^2\right). \tag{2.5}$$

Here, $g(D)$ is a degradation function which is dependent on the damage variable D (in this work $g(D) = (1-D)^2$), $\sigma_{\mathrm{y}0}$ is the initial yield stress, α is an internal plastic hardening variable, l denotes an internal length parameter, $g_{\mathrm{c}}^{\mathrm{e}}$ is the fracture energy in the elastic brittle case (i.e., for $\sigma_{\mathrm{y}0} \to \infty$) and $\beta \in [0, 1]$ is a material parameter, which is further explained below. Moreover, $\| \bullet \|$ is the L2-norm, ψ_{p} denotes the plastic hardening potential and the elastic energy ψ_{e} is split into a tension part $\psi_{\mathrm{e}+}$ and a compression part $\psi_{\mathrm{e}-}$ which are assumed to be given by (compare [8])

$$\begin{aligned} \psi_{\mathrm{e}+} &= \frac{\lambda}{2}\langle \mathrm{tr}(\varepsilon^{\mathrm{e}})\rangle^2 + \mu\varepsilon^{\mathrm{e}} : \varepsilon^{\mathrm{e}}, \\ \psi_{\mathrm{e}-} &= \frac{\lambda}{2}\langle -\mathrm{tr}(\varepsilon^{\mathrm{e}})\rangle^2, \end{aligned} \tag{2.6}$$

with λ and μ as the first and second Lamé-constants, respectively, and $\langle x \rangle = (x + |x|)/2$.

For $D = 0$ (undamaged material), the free energy thus corresponds to the geometrically nonlinear J_2-flow theory with isotropic hardening presented in [8][1], which has been used and extended by numerous authors. In addition, we include the possibility to model a purely energetic yield stress σ_{y0} (for $\beta = 1$ in Eq. (2.5)), a purely dissipative yield stress (for $\beta = 0$, see also the dissipation potential in Eq. (2.10) below) and any intermediate choice. This allows, for example, to properly account for a given Taylor-Quinney coefficient. The storage of elastic and plastic energy contributions is assumed to drive the damage of the material, except for the compression part ψ_{e-} (Eq. (2.6)). Thus, they are multiplied by the degradation function $g(D)$ in Eq. (2.5), i.e., the related energy is released when the material is damaged. Finally, the last summand in Eq. (2.5) is consistent with the regularized crack surface energy for the elastic brittle case (see, e.g., [36]), which is well-known to be consistent (in the sense of Γ-convergence) with the Griffith-model.

The hardening potential ψ_p is assumed to be a convex function with

$$q = \frac{\partial \psi_p}{\partial \alpha} \geq 0. \tag{2.7}$$

For example, in the simple case of linear hardening

$$\psi_p(\alpha) = \frac{H_p}{2}\alpha^2 \tag{2.8}$$

with hardening modulus H_p. Using Eqs. (2.5) and (2.6), it is seen later that the Kirchhoff-stress $\boldsymbol{\tau}$ is given by

$$\boldsymbol{\tau} = 2\mathbf{b}^e \frac{\partial \psi_e}{\partial \mathbf{b}^e} = \frac{\partial \psi_e}{\partial \varepsilon^e} = g(D)\Big(\underbrace{\lambda \langle \mathrm{tr}(\varepsilon^e)\rangle \mathbf{I} + 2\mu \varepsilon^e}_{\boldsymbol{\tau}_{0+}} \Big) - \lambda \langle -\mathrm{tr}(\varepsilon^e)\rangle \mathbf{I}. \tag{2.9}$$

The dissipation potential ϕ is assumed to be given by (compare [43])

$$\phi(\mathbf{D}^p, \dot{\alpha}) = \begin{cases} \sqrt{\frac{2}{3}}(1-\beta)\sigma_{y0}\|\mathbf{D}^p\| & \text{if } \dot{\alpha} \geq \sqrt{\frac{2}{3}}\|\mathbf{D}^p\| \wedge \mathrm{tr}(\mathbf{D}^p) = 0, \\ \infty & \text{else.} \end{cases} \tag{2.10}$$

Here, the '∞'-branch ensures that: 1) $\mathrm{tr}(\mathbf{D}^p) = 0$, which corresponds to the aforementioned plastic incompressibility constraint and 2) $\dot{\alpha} \geq \sqrt{2/3}\|\mathbf{D}^p\|$.

The free energy density ψ and the dissipation potential ϕ enable the construction of an integral incremental potential Π (given at a later point), the

[1] It is noted that the J_2-flow theory is only one application of the framework presented in [8].

minimization conditions of which deliver all required model equations. This minimization also applies to the time-discrete counterpart Π_Δ of Π. In the case of infinitesimal time steps, the time-continuous and time-discrete models coincide. Therefore, we restrict all further steps to the time-discrete setting, noting that the time-continuous theory is recovered in the aforementioned limit case. The model equations, as summarized in Box 1, are derived below together with suitable boundary conditions. The equations comprise the linear momentum balance equation, an analogous equation related to D, which we interpret as micro-force balance in the sense of Gurtin [28], the elastic law, the yield criterion and the flow rule. Note from the yield criterion that the material parameter β enables a split of the initial yield stress $\sigma_{\mathrm{y}0}$ into a part $\beta\sigma_{\mathrm{y}0}$, being degraded by the function $g(D)$ and a constant part $(1-\beta)\sigma_{\mathrm{y}0}$.

Box 1: Model equations. Here, P denotes the first Piola-Kirchhoff stress, ρ_0 is the mass density in the reference configuration, b is the body force and 'Δ' denotes the Laplace operator.

1. Quasi-static linear momentum balance:

$$\mathbf{0} = \mathrm{Div}\,\mathbf{P} + \rho_0\mathbf{b}; \qquad \text{with } \mathbf{P} = \boldsymbol{\tau}\mathbf{F}^{-\top} \text{ and } \boldsymbol{\tau} = \tfrac{\partial \psi_{\mathrm{e}}}{\partial \varepsilon^{\mathrm{e}}}.$$

2. Micro-force balance:

$$0 = g'(D)\big(\psi_{\mathrm{e}+}(\varepsilon^{\mathrm{e}}) + \beta\sigma_{\mathrm{y}0}\alpha + \psi_{\mathrm{p}}(\alpha)\big) + g_{\mathrm{c}}^{\mathrm{e}}\big(\tfrac{D}{l} - l\Delta D\big).$$

3. Yield criterion

$$f = g(D)\left(\|\boldsymbol{\tau}'_{0+}\| - \sqrt{\tfrac{2}{3}}(\beta\sigma_{\mathrm{y}0} + q)\right) - \sqrt{\tfrac{2}{3}}(1-\beta)\sigma_{\mathrm{y}0} \leq 0.$$

4. Flow rule (with plastic multiplier γ):

$$\mathcal{L}_{\mathrm{v}}\mathbf{b}^{\mathrm{e}} = \mathbf{R}^{\mathrm{e}}\mathbf{D}^{\mathrm{p}}\mathbf{R}^{\mathrm{e}\top} = \gamma\tfrac{\boldsymbol{\tau}'_{0+}}{\|\boldsymbol{\tau}'_{0+}\|},$$

where $\mathcal{L}_{\mathrm{v}}\mathbf{b}^{\mathrm{e}} = \mathbf{F}\dot{\overline{\mathbf{C}^{\mathrm{p}-1}}}\mathbf{F}^{\top} = \dot{\mathbf{b}}^{\mathrm{e}} - \mathbf{l}\mathbf{b}^{\mathrm{e}} - \mathbf{b}^{\mathrm{e}}\mathbf{l}^{\top}$ is the Lie derivative of $\mathbf{b}^{\mathrm{e}}$.

It is noted that without damage ($D = 0$, $g(D) = 1$), the yield criterion (Box 1) is identical to the one of the aforementioned J_2-flow theory with isotropic hardening. For the choice $\beta = 1$, the yield criterion takes the same form as in a model without damage (since then, the yield criterion may be divided by $g(D)$ without consequences). This choice thus corresponds to the 'effective stress' concept (see [44]), and elasticity and plasticity together form the driving force[2] for damage (often the plastic energy significantly exceeds the elastic energy). In contrast, for $\beta < 1$, the influence of plasticity on damage decreases. For example, for the extreme (usually unrealistic) case $\beta = 0$ and ideal plasticity (no hardening), damage would result merely from elastic energy storage, as the

[2]Formally, one may consider the first summand of the right hand side of the micro-force balance in Box 1 as damage driving force due to elastic and plastic energy storage.

driving force for damage in the micro-force balance (see Box 1) would then read $g'(D)\psi_{\mathrm{e}+}(\varepsilon^{\mathrm{e}})$.

REMARK. As an alternative to Eq. (2.5), one may use for the gradient part a micromorphic formulation [45] by introducing a micromorphic counterpart D^{χ} of the damage variable D and an additional energy contribution $H^{\chi}(D^{\chi}-D)^2/2$. This leads to an equivalent model in the case $H^{\chi}\to\infty$. In practice, one typically penalizes deviations of the two variables by choosing sufficiently high values for H^{χ}. A material subroutine containing the code including the related algorithmic details is published together with this manuscript.

2.3. Time discretization

2.3.1. Kinematics. In the following, the index $(\bullet)^{\mathrm{tr}}$ denotes the trial state, the index $(\bullet)_{\mathrm{n}}$ denotes quantities from the previous time step and the index $(\bullet)_{\mathrm{n+1}}$ denotes quantities of the current time step. The latter is omitted in most cases for simplicity. The trial state describes the local state, assuming that no plastic deformation occurs in the current time step:

$$\mathbf{F}^{\mathrm{etr}}=\mathbf{F}\mathbf{F}_{\mathrm{n}}^{\mathrm{p}-1},\qquad \mathbf{b}^{\mathrm{etr}}=\mathbf{F}^{\mathrm{etr}}\mathbf{F}^{\mathrm{etr}\top}=\mathbf{F}\mathbf{C}_{\mathrm{n}}^{\mathrm{p}-1}\mathbf{F}^{\top}. \tag{2.11}$$

Additionally, in analogy to the definition of the polar decomposition in (2.1) and the Cauchy–Green tensors in (2.2), the following tensors are defined

$$\mathbf{f}^{\mathrm{p}}=\mathbf{F}^{\mathrm{p}}\mathbf{F}_{\mathrm{n}}^{\mathrm{p}-1}=\mathbf{r}^{\mathrm{p}}\mathbf{u}^{\mathrm{p}},\qquad \mathbf{c}^{\mathrm{p}}=\mathbf{f}^{\mathrm{p}\top}\mathbf{f}^{\mathrm{p}},\qquad \mathbf{b}^{\mathrm{p}}=\mathbf{f}^{\mathrm{p}}\mathbf{f}^{\mathrm{p}\top}=\mathbf{r}^{\mathrm{p}}\mathbf{c}^{\mathrm{p}}\mathbf{r}^{\mathrm{p}\top}. \tag{2.12}$$

Finally, the following relations can be found

$$\mathbf{F}^{\mathrm{e}}=\mathbf{V}^{\mathrm{e}}\mathbf{R}^{\mathrm{e}}=\mathbf{F}^{\mathrm{etr}}\mathbf{f}^{\mathrm{p}-1},\qquad \mathbf{b}^{\mathrm{e}}=\mathbf{F}^{\mathrm{etr}}\mathbf{c}^{\mathrm{p}-1}\mathbf{F}^{\mathrm{etr}\top}. \tag{2.13}$$

2.3.2. Time-discrete global incremental potential. A possible time discrete version of the dissipation potential (see Eq. 2.10), being consistent with an exponential map based update of the plastic deformation (e.g., [6, 7], is given by (compare [12])

$$\phi_{\Delta}=\begin{cases}\sqrt{\frac{2}{3}}(1-\beta)\sigma_{\mathrm{y0}}\|\frac{1}{2}\ln\mathbf{c}^{\mathrm{p}}\| & \text{if } \Delta\alpha\geq\sqrt{\frac{2}{3}}\|\frac{1}{2}\ln\mathbf{c}^{\mathrm{p}}\|\wedge\det\mathbf{c}^{\mathrm{p}}=0,\\ \infty & \text{else.}\end{cases} \tag{2.14}$$

The time discrete total potential π_{Δ} is given by

$$\pi_{\Delta}=\psi-\psi_{\mathrm{n}}-\phi_{\Delta},\qquad \pi=\lim_{\Delta t\to 0}\frac{1}{\Delta t}\pi_{\Delta}. \tag{2.15}$$

REMARK. It is noted that, due to Eq. (2.7) (which implies $\partial\psi/\partial\alpha\geq 0$) the minimization of π_{Δ} with respect to α implies that α 'tries to be as small as

possible'. In combination with the inequality constraint $\Delta\alpha \geq \sqrt{2/3}\|\frac{1}{2}\ln \mathbf{c}^{\mathrm{p}}\|$ in Eq. (2.14), the equality sign applies, i.e., $\Delta\alpha = \sqrt{2/3}\|\frac{1}{2}\ln \mathbf{c}^{\mathrm{p}}\|$ or $\dot{\alpha} = \sqrt{2/3}\|\mathbf{D}^{\mathrm{p}}\|$ in the time-continuous case. Thus, α represents the conventional equivalent plastic strain measure which is used to model isotropic hardening.

Further, we define the global incremental potential

$$\Pi_{\Delta} = \int_{V_0} \pi_{\Delta}\,\mathrm{d}V - \int_{V_0} \rho_0 \boldsymbol{b}\cdot\boldsymbol{u}\,\mathrm{d}V - \int_{\partial V_{0t}} \hat{\boldsymbol{t}}\cdot\boldsymbol{u}\,\mathrm{d}A \tag{2.16}$$

with the traction vector $\hat{\boldsymbol{t}}$, being prescribed on the traction boundary ∂V_{0t}, while the displacements $\boldsymbol{u}$ are assumed to be prescribed on the Dirichlet boundary ∂V_{0u}. The variations of Π_{Δ} with respect to $\boldsymbol{u}$ and D yield the weak form of the first two equations in Box 1:

$$\int_{V_0} \underbrace{\boldsymbol{\tau} : \boldsymbol{d}_{\delta}}_{\boldsymbol{P}:\delta\boldsymbol{F}}\,\mathrm{d}V - \int_{V_0} \rho_0 \boldsymbol{b}\cdot\delta\boldsymbol{u}\,\mathrm{d}V - \int_{\partial V_{0t}} \hat{\boldsymbol{t}}\cdot\delta\boldsymbol{u}\,\mathrm{d}A = 0, \tag{2.17}$$

$$\int_{V_0} \left(\frac{\partial \pi_{\Delta}}{\partial D}\delta D + \frac{\partial \pi_{\Delta}}{\partial \mathrm{Grad}(D)}\cdot \mathrm{Grad}(\delta D) \right) \mathrm{d}V = 0, \tag{2.18}$$

with $\boldsymbol{d}_{\delta} = \mathrm{sym}(\delta\boldsymbol{F}\boldsymbol{F}^{-1})$ and $\boldsymbol{P} = \partial\psi/\partial\boldsymbol{F}$. The displacement variation $\delta\boldsymbol{u}$ is assumed to vanish on ∂V_{0u}. It is then a standard exercise to show that $\boldsymbol{\tau} = 2\mathbf{b}^{\mathrm{e}}\partial\psi_{\mathrm{e}}/\partial\mathbf{b}^{\mathrm{e}} = \partial\psi_{\mathrm{e}}/\partial\varepsilon^{\mathrm{e}}$ (see also [8]) and that[3] equations 1 and 2 in Box 1 as well as the boundary conditions $\hat{\boldsymbol{t}} = \boldsymbol{P}\boldsymbol{N}$ on ∂V_{0t} and $\mathrm{Grad}(D)\cdot\boldsymbol{N} = 0$ on ∂V_0 (where $\boldsymbol{N}$ is the external normal vector) follow from the stationarity conditions (2.17) and (2.18) of Π_{Δ} with respect to $\boldsymbol{u}$ and D. Finally, it is noted that also mixed boundary conditions are possibile (i.e., ∂V_{0t} and ∂V_{0u} overlap), if the displacement is prescribed in certain coordinate directions and the tractions in the remaining directions in the overlap region.

2.4. Local stationarity conditions

The internal variables are obtained from a local minimization of π_{Δ} (see below). Using the definitions (2.11) and (2.12) one can formulate

$$\mathbf{b}^{\mathrm{etr}} = \mathbf{F}^{\mathrm{e}}\mathbf{b}^{\mathrm{p}}\mathbf{F}^{\mathrm{e}\top} = \mathbf{V}^{\mathrm{e}}\mathbf{R}^{\mathrm{e}}\mathbf{b}^{\mathrm{p}}\mathbf{R}^{\mathrm{e}\top}\mathbf{V}^{\mathrm{e}} = \mathbf{b}^{\mathrm{e}}\mathbf{R}^{\mathrm{e}}\mathbf{b}^{\mathrm{p}}\mathbf{R}^{\mathrm{e}\top}, \tag{2.19}$$

where the last equality follows from the fact that $\mathbf{b}^{\mathrm{e}} = (\mathbf{V}^{\mathrm{e}})^2$ and $\mathbf{R}^{\mathrm{e}}\mathbf{b}^{\mathrm{p}}\mathbf{R}^{\mathrm{e}\top}$ are coaxial (with $\mathbf{b}^{\mathrm{p}} = \mathbf{f}^{\mathrm{p}}\mathbf{f}^{\mathrm{p}\top}$, see Eq. (2.12)). For completeness, a derivation of the aforementioned coaxiality is given in Appendix B.

[3] By application of the chain rule and the Gauss theorem.

As a consequence, one may write (e.g., [8])

$$\varepsilon = \varepsilon^{\mathrm{etr}} = \frac{1}{2}\ln \mathbf{b}^{\mathrm{etr}} = \frac{1}{2}\ln \mathbf{b}^{\mathrm{e}} + \frac{1}{2}\ln \mathbf{R}^{\mathrm{e}}\mathbf{b}^{\mathrm{p}}\mathbf{R}^{\mathrm{e}\top} = \varepsilon^{\mathrm{e}} + \varepsilon^{\mathrm{p}} \tag{2.20}$$

with

$$\mathrm{tr}(\varepsilon^{\mathrm{p}}) = 0 \quad \Leftrightarrow \quad \det \mathbf{c}^{\mathrm{p}} = 0. \tag{2.21}$$

Note that in the equations above, $\varepsilon^{\mathrm{etr}}$ is an incremental algorithmic strain measure and not related to the total deformation[4]. Furthermore, with (2.6) it is possible to reformulate (2.5) as follows

$$\begin{aligned}\psi = g(D)\left(\frac{\lambda}{2}\langle \mathrm{tr}(\varepsilon^{\mathrm{e}})\rangle^2 + \mu\varepsilon^{\mathrm{e}} : \varepsilon^{\mathrm{e}} + \beta\sigma_{\mathrm{y0}}\alpha + \psi_{\mathrm{p}}(\alpha)\right) + \frac{\lambda}{2}\langle -\mathrm{tr}(\varepsilon^{\mathrm{e}})\rangle^2 \\ + \frac{1}{2}g_{\mathrm{c}}^{\mathrm{e}}\left(\frac{D^2}{l} + l\|\mathrm{Grad}(D)\|^2\right).\end{aligned} \tag{2.22}$$

Since π_Δ is to be minimized with respect to $\Delta\alpha$, the inequality in the 'if'-branch of Eq. (2.14), together with Eq. (2.7), yields

$$\Delta\alpha = \sqrt{\frac{2}{3}}\left\|\frac{1}{2}\ln \mathbf{c}^{\mathrm{p}}\right\| = \sqrt{\frac{2}{3}}\|\varepsilon^{\mathrm{p}}\|, \tag{2.23}$$

where it has been exploited that $\|\ln \mathbf{c}^{\mathrm{p}}\| = \|\ln \mathbf{r}^{\mathrm{p}}\mathbf{c}^{\mathrm{p}}\mathbf{r}^{\mathrm{p}\top}\| = \|\ln \mathbf{b}^{\mathrm{p}}\| = \|2\varepsilon^{\mathrm{p}}\|$. Thus, the time-discrete dissipation potential from (2.15) becomes

$$\phi_\Delta = \sqrt{\frac{2}{3}}(1-\beta)\sigma_{\mathrm{y0}}\|\varepsilon^{\mathrm{p}}\|, \tag{2.24}$$

if one constrains ε^{p} to be traceless. Clearly, the total potential π_Δ (Eq. (2.15)) is formally equivalent with its small strain counterpart [8, 12]. A simple calculation then shows that minimizing the potential with constraints

$$\inf_{\varepsilon^{\mathrm{p}}=\varepsilon^{\mathrm{p}\prime}} \pi_\Delta(\varepsilon, D, \varepsilon^{\mathrm{p}}) = \inf_{\Delta\gamma\geq 0}\ \inf_{\substack{\mathbf{n}=\mathbf{n}'\\ \|\mathbf{n}\|=1}} \pi_\Delta(\varepsilon, D, \Delta\gamma\mathbf{n}), \tag{2.25}$$

yields the flow rule

$$\varepsilon^{\mathrm{p}} = \Delta\gamma\mathbf{n}, \tag{2.26}$$

[4]Further note that (compare, e.g., [8]) the tensor $\mathbf{R}^{\mathrm{e}}\mathbf{b}^{\mathrm{p}}\mathbf{R}^{\mathrm{e}\top}$ is unique, even if the elastoplastic split remains unspecified upon a rigid body rotation/proper orthogonal tensor $\mathbf{Q}$, i.e., with $\mathbf{F} = \mathbf{F}^{\mathrm{e}}\mathbf{F}^{\mathrm{p}} = \mathbf{F}^{\mathrm{e}}\mathbf{Q}^\top\mathbf{Q}\mathbf{F}^{\mathrm{p}} = \hat{\mathbf{F}}^{\mathrm{e}}\hat{\mathbf{F}}^{\mathrm{p}}$, $\hat{\mathbf{F}}^{\mathrm{e}} = \mathbf{V}^{\mathrm{e}}\hat{\mathbf{R}}^{\mathrm{e}} = \mathbf{V}^{\mathrm{e}}\mathbf{R}^{\mathrm{e}}\mathbf{Q}^\top = \mathbf{F}^{\mathrm{e}}\mathbf{Q}^\top$ and $\hat{\mathbf{b}^{\mathrm{p}}} = \hat{\mathbf{F}^{\mathrm{p}}}\hat{\mathbf{F}^{\mathrm{p}}}^\top = \mathbf{Q}\mathbf{b}^{\mathrm{p}}\mathbf{Q}^\top$, it follows that $\hat{\mathbf{R}^{\mathrm{e}}}\hat{\mathbf{b}^{\mathrm{p}}}\hat{\mathbf{R}^{\mathrm{e}}}^\top = \mathbf{R}^{\mathrm{e}}\mathbf{b}^{\mathrm{p}}\mathbf{R}^{\mathrm{e}\top}$.

where $\mathbf{n}$ is the plastic flow direction given by

$$\mathbf{n} = \frac{\varepsilon^{\mathrm{e}\prime}}{\|\varepsilon^{\mathrm{e}\prime}\|} = \frac{\varepsilon'}{\|\varepsilon'\|} = \frac{\tau^{\mathrm{tr}\prime}}{\|\tau^{\mathrm{tr}\prime}\|}. \tag{2.27}$$

The yield criterion f represents the minimization condition with respect to $\Delta\gamma \geq 0$:

$$f = -\frac{\partial \pi_{\Delta}}{\partial \Delta\gamma} = g(D)\left(\| \underbrace{2\mu\varepsilon^{\mathrm{e}\prime}}_{\boldsymbol{\tau}'_{0+}} \| - \sqrt{\frac{2}{3}}(\beta\sigma_{\mathrm{y0}} + q) \right) - \sqrt{\frac{2}{3}}(1-\beta)\sigma_{\mathrm{y0}} \leq 0, \tag{2.28}$$

which completes the model description.

For the global Newton scheme, the algoritmic tangent operators are also required. These are discussed in Appendix C.

3. Materials and methods

Epoxy resins are highly competitive among thermoset materials in industrial applications owing to their excellent thermal and chemical resistance as well as the high tensile strength and stiffness they exhibit. However, they suffer from a main drawback restricting their usage in many practical applications which is their limited resistance to the initiation and the growth of existing cracks. Therefore, researchers have become increasingly interested in the enhancement of the toughness of epoxy resins to ensure their reliability [46]. Several studies have been carried out for this purpose by adopting the same solution which is the addition of a stiff or soft second phase to the resin [47]. A stiff second phase, used to improve the toughness of epoxies, can be organic or inorganic. The latter is widely used in this purpose such as carbon and glass fibers. Soft reinforcing particles often used are compliant rubbery particles.

3.1. Core-shell rubber particles modified epoxy

The rubber-toughening technique includes two conventional methods. In the first one, the rubber is incorporated initially into the matrix as a miscible liquid, and then using a reactive additive, the second phase particles are formed. In this kind of compounds, the volume fraction and the size of the rubber particles are influenced by the degree of compatibility between the two phases and also the kinetics of gelation [48] which makes the control of the compound morphology very difficult. This could be considered as a critical drawback as the fracture toughness depends highly on the morphology of the compounds [49]. In the second method, the second phase is preformed and then included in the resin. This second phase is identified as core-shell particles with a rubbery core and

a thin layer of a glassy shell. The rubbery core ensures the improvement of the toughness. The outer glassy shell is designed to be compatible with the resin, it improves the dispersion of the rubbery particles within the matrix and prevents their coalescence [50].

The control of the particles' size and the volume fraction of the second phase is possible if core-shell particles are incorporated. This makes this modifiers generation one of the most preferred ones for the purpose of polymer toughening [49]. Therefore, in the present study, interest has been granted to investigate the extent of the contribution of this filler to the toughening of the epoxy. Basically, the 'toughening' is the increase of the ability of the material to absorb energy and deform plastically before the fracture. The incorporation of rubbery particles in the epoxy resin involves the apparition of several energy dissipative mechanisms when the compound is loaded, such as shear banding in the epoxy matrix between the rubbery particles, the cavitation of the rubbery particles, the plastic deformation, the growth of the voids initiated by cavitation of the particles and the rubber-bridging mechanism [50–52]. As reported in [50], the particles' cavitation is not only a dissipative mechanism but also the mechanism that triggers the whole toughening process. Indeed, the voids resulting from the cavitation of the rubber particles act as stress concentrators and relieve the triaxial stress state ahead of cracks. Therefore, the fracture of the compound is delayed by allowing the plastic void growth and the shear banding in the matrix instead.

The overview article [53] discusses computational models for the fundamental toughening mechanisms 'crazing' and 'shear yielding' in rubber-particle enhanced polymers including cavitation, void growth and coalescence.

As the toughening is basically equivalent to the energy absorbed through the plastic growth of the voids and the shear yielding in the matrix between these voids, it is obvious to assume that the improvement of toughness depends highly on the volume fraction of the particles, on their size as well as their distribution in the matrix. The effect of these parameters on the behavior of the rubber-epoxy compounds is commonly examined by several experimental studies. The review [49] outlines the most important findings of these investigations. In the same context, this study aims to characterize numerically the behavior of the epoxy being modified with rubbery particles for different micro-structures.

It is obvious that a detailed model would ensure the identification of the various energy-dissipating mechanisms involved when rubbery nano-particles are added as well as the quantification of their contributions to the toughening to epoxy. However, as described, e.g. in [51] and [52], the plastic shear banding in the epoxy matrix and the plastic void growth are the main toughening mechanisms. This simplifying assumption has been adopted in the present study and the cavitation mechanism has been neglected. Indeed, the particles have been represented as spherical voids dispersed in the matrix. Moreover, it has been re-

ported that rubber particles cavitate at a relatively low-stress level [52] and have a stiffness much smaller than that of the surrounding polymer (Young's modulus of the rubber phase is around 4 MPa, [54]). This supports the assumption of the representation of the particles as voids. The same approach has been adopted in several studies [55–58].

Therefore, to characterize the behavior of the overall CSR/epoxy composite only one component has been considered which is the epoxy matrix, whose typical properties are presented in Table 1. And the investigation of the effect of the microstructural morphology on its mechanical properties has involved the variation of the dimensions, the volume fraction, and the distribution of the voids representing the incorporated particles, in addition to the variation of the epoxy properties initially considered.

Table 1. Material properties of the epoxy matrix of the CSR/epoxy composite.

Young's modulus E [MPa]	Initial yield stress σ_{y0} [MPa]	Elastic energy release rate g_c^e [J/m^2]	Poisson's ratio ν
3000	80	50	0.35
Hardening modulus H_p [MPa]	**Internal length l [μm]**	**Coupling modulus H^χ [MPa]**	**Yield stress parameter β**
10	0.0125	10^6	1

3.2. Carbon fiber reinforced epoxy

The performance of FRP (fiber-reinforced polymer) composite materials predominantly depends on their constituent elements and manufacturing techniques. Therefore, various manufacturing techniques are used worldwide in the industry to fabricate optimized FRP composite materials for the desired application [59]. The filament winding is an automated composite fabrication technique competitive for the manufacturing of thick-walled components, enabling a fast production with few defects. This technique involves continuous winding of impregnated rovings of fibers in a resin bath just prior to application on a «winding-core» while keeping them in tension. Despite the competitiveness of this technique, the presence of manufacturing defects in the material is unavoidable. Voids are one of the most significant defects that could be generated during the manufacturing of carbon fiber reinforced polymer (CFRP) composites which represent regions unfilled with polymer and fibers. Their significance is due to their high formation probability as well as to their considerable effect on the mechanical properties of the composite and their contribution to the creation of new damage mechanisms leading to failure. As a result of their importance, voids are one of the most studied manufacturing defects. A numerical attempt

to highlight the effect of this defect on the behavior of the CFRP material has been made by the consideration of holes in different sizes and fractions when modeling the CFRP microstructure.

In contrast to the CSRP (core-shell rubber particles) microstructure model, the CFRP-model involves the definition and the implementation of two materials. Indeed, microscopic unidirectional cylinders have been included in the matrix. In addition to circular fibers, elliptical reinforcing fibers have been considered in order to investigate the effect of the fiber shape on the overall composite behavior. The volume fraction of the fibers also has been varied to investigate its effect on the composite properties. The mechanical properties considered to simulate the behavior of this material are gathered in Table 2. The epoxy properties are the same as for the CSR/epoxy composite (except for the internal length which is now $l = 0.0625$ μm)

Table 2. Elastic material properties of the constituents (matrix and fibers) of the CFRP-model.

	Carbon fibers	Epoxy
Diameter	7 μm	–
Volume fraction	60%	40%
Longitudinal Young's modulus	239000 MPa	3000 MPa
Transverse Young's modulus	15000 MPa	–
Longitudinal shear modulus	20000 MPa	–
Transverse shear modulus	6000 MPa	–
Longitudinal Poisson's ratio	0.2	0.35
Transverse Poisson's ratio	0.25	–

3.3. Woven fiber composite

The third material characterized is a woven glass fiber reinforced epoxy composite. The manufacturing of this composite material consists of the continuous weaving of glass fiber rovings in two mutually perpendicular directions after being embedded in the epoxy resin. This composite provides bidirectional properties highly dependent on the microstructural parameters of the reinforcing fibers such as the type, diameter, volume fraction and density [60]. Therefore, simulations were performed to investigate the stress response and resistance to fracture of a woven structure of rovings embedded in a brittle matrix as well as the influence of the rovings' vertical and lateral thickness on the overall woven composite. The effect of the mechanical properties of each component (matrix and rovings) on the failure behavior of the overall composite has been also highlighted. The major material properties chosen in this study are given in Table 3.

Table 3. Material properties of epoxy matrix (M) and rovings (R) as components of the woven fiber composite.

Young's modulus		Elastic energy release rate	Poisson's ratio	
E_M [MPa]	E_R [MPa]	g_c^e [J/m^2]	ν_M	ν_R
3039	63647	133	0.36	0.213

4. Computational models

Computational modeling of composites with periodic microstructure can be performed by the consideration of a periodic unit cell of the material which is a small volume over which computation are made in order to estimate the response of the whole composite behavior. Therefore a unit cell has been used to conduct all simulations to investigate the impact of different material and microstructural parameters on the behavior of the composites. Such unit cells

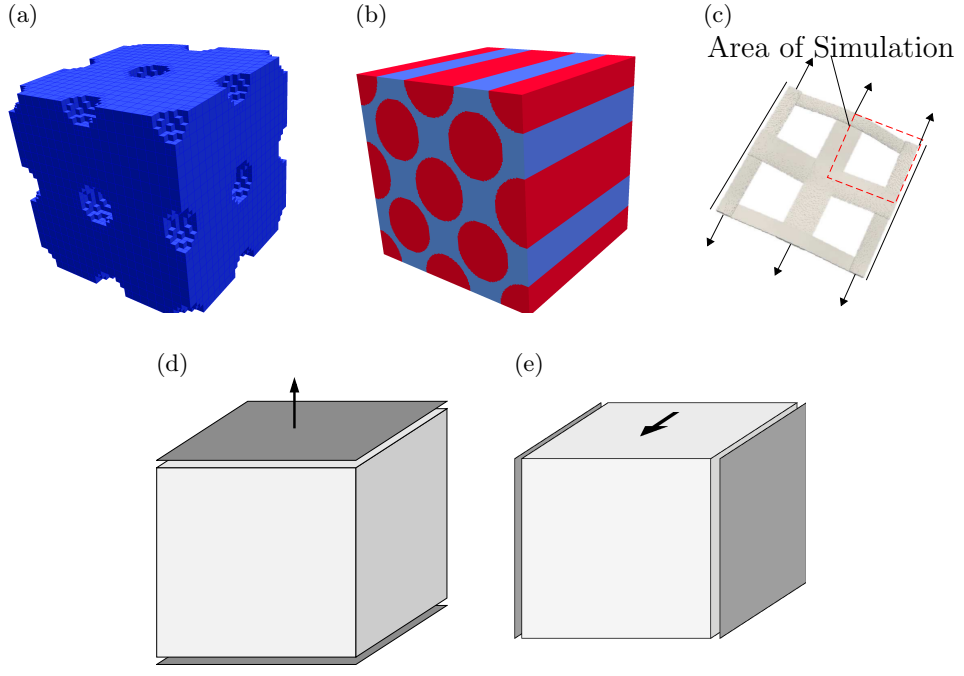

Fig. 1. Materials unit cells: (a) 0.5µm×0.5µm×0.5µm cubic unit cell of the epoxy modified with spherical CSR nano-particles (modelled as voids) of 50nm radius, (b) model of the CFRP micro-structure with 60% of circular fibers, (c) model of the woven fiber composite under uniaxial tension and constrained transversal contraction, (d) tensile boundary conditions (BCs) with free lateral contractions (applied to (a) and (b)) and (e) shear boundary conditions (applied to (b)). The arrows indicate prescribed displacements and the dark regions constant displacements perpendicular to the specific surfaces. More details on the boundary conditions can be found in the specific simulation sections below.

should contain sufficient information about the reinforcing inclusions' (particles or fibers) size, volume fraction, type, orientation, and spatial distribution.

Indeed, to characterize the influence of different microstructural and material parameters on the overall behavior of each material, comparative studies have been carried out by the implementation of a Fortran code capable of incorporating inclusions of different shapes and sizes in the composite unit cell according to the distribution and the volume fraction desired. The finite element discretizations of the microscopic unit cell modeled to simulate the behavior of the CSR particles modified epoxy, the carbon fibers reinforced epoxy and the woven fiber-reinforced epoxy are shown respectively in Figs. 1a to 1c.

Concerning the boundary conditions, a tensile loading has been imposed in terms of displacements on unit cells of the three micro-structures. Trilinear hexahedral elements with reduced integration and hourglass stabilization have been used. Subroutines where the mechanical constitutive behavior of the material is defined have also been modified depending on the composite microstructure to characterize. Indeed, several material and finite element subroutines have been implemented based on the material model developed and presented above allowing for the description of the elasto-plastic geometrically nonlinear behavior of the materials involved. Carbon fibers in the CFRP microstructure have been assumed to be transversally isotropic and its five independent elastic constants are listed in Table 2, while the glass fibers reinforcing the woven fiber composite have been considered isotropic. The epoxy matrix has been modeled as an isotropic elastic/elastoplastic solid for the three microstructures. All simulations are executed by the finite element analysis software FEAP [61] and use a parallel

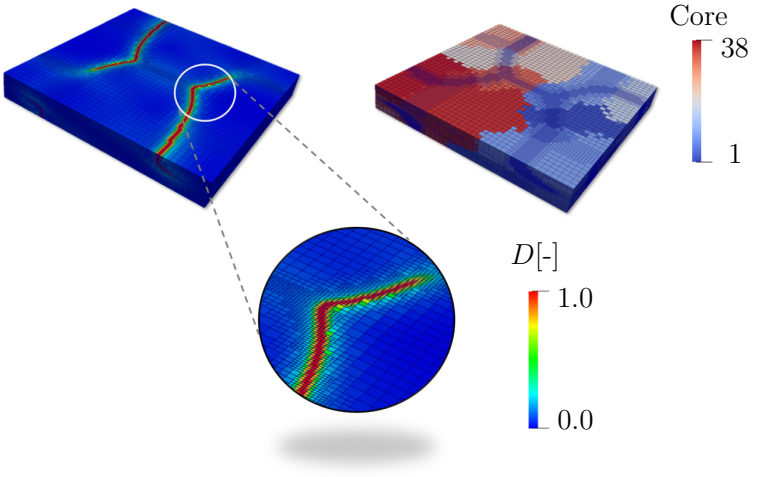

FIG. 2. Investigation of crack formation with adaptive mesh algorithm and parallelization.

build (38 cores). To enable a refined numerical resolution, an adaptive meshing technique has been applied at the level of cracked regions. Figure 2 shows an exemplary section of the mesh adopted to investigate the failure behavior of the woven fiber composite. It could be clearly noticed that the mesh is refined only at regions of crack formation (damage variable D high) which are, inter alia, regions of the high level of stress concentration at the crack tip. This same figure highlights as well the use of the parallel build with 38 cores.

5. Simulations

5.1. Application of the model to woven glass fiber reinforced epoxy

Simulations were performed to investigate the stress response and resistance to fracture of a woven structure of rovings embedded in a brittle matrix. Therefore, a displacement controlled uniaxial tension test with one constrained and one fully (traction-) free transversal contraction is performed on the 3-dimensional modelled structure depicted in Fig. 1c. More precisely, the boundary conditions applied to the unit cell in Fig. 1c were such that in the tensile direction ($\hat{=}x$-direction), the displacements in this direction on two opposed faces (with face normals $\pm e_x$[5]) were prescribed. The displacements in the lateral directions on these faces were free. On the top and bottom faces, zero-traction boundary conditions were applied and on the remaining faces (left and right), symmetry conditions were applied (compare Fig. 1c). For simplicity, matrix and rovings are modelled as isotropic materials. The chosen material parameters are given in Table 4, except for the cases where other parameters are explicitly given in the text. Due to the exploitation of symmetries only one quarter of the structure is meshed. Note that due to the thin nature of the sample the hexahedral elements are chosen to be significantly smaller in the dimension perpendicular to the plane. Since in this section no plastic deformations are considered, the small strain[6] micromorphic model is applied. Plastic deformations are neglected, as practically applied epoxies often show negligible plastic deformations in tensile experiments conducted on the mm-scale (the scale of the woven composite), while significant elastoplastic deformations are observed on smaller scales (e.g. [62]). Large deformations are considered in a later section.

The monitoring of strains and stresses in the rovings, cracking in the matrix and the texture over the course of the simulation are visualized in Fig. 3. At the intersection of the rovings the maximum stresses and the initiation of cracking

[5]Here, e_x is the unit vector in x-direction.

[6]The small strain model is described by Eq. (2.22) (with $\sigma_{y0} \to \infty \Rightarrow \alpha = 0, \boldsymbol{\varepsilon}^p = \mathbf{0}$), where now $\boldsymbol{\varepsilon}$ is the infinitesimal strain tensor, in combination with the small strain counterparts of the balance equations in Box 1 (basically replacing $\boldsymbol{P}$ by $\boldsymbol{\sigma}$).

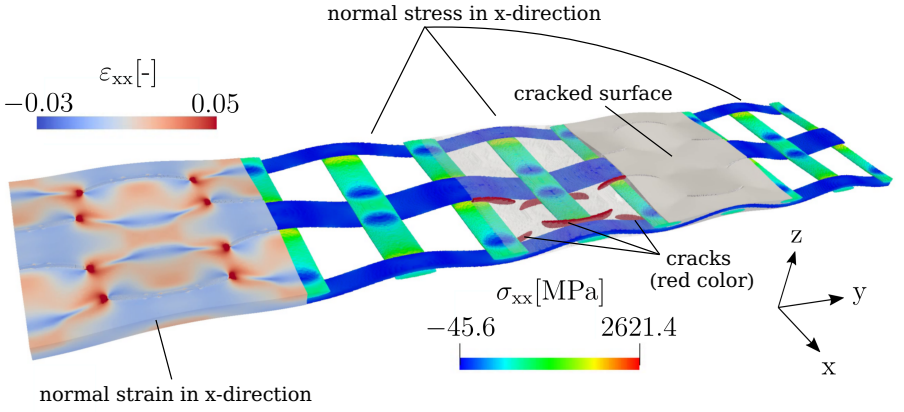

FIG. 3. Simulation of woven roving model with monitoring of strains, stresses and cracks. Internal cracks are shown in the center (front) in red color.

in the matrix can be observed. This location of the matrix crack onset is in good agreement with the simulations of the authors of [63] (compare also [64]), who used an anisotropic damage model, but did not include gradient effects. The maximum strains are found at the tips of the growing cracks.

Table 4. Material parameters of matrix (M) and rovings (R), the latter ones assumed purely elastic (no damage).

λ_M [MPa]	μ_M [MPa]	λ_R [MPa]	g_c^e[J/m^2]	μ_R [MPa]	l [mm]	H^χ[MPa]
3085.9	1111.11	19489	133	26233	0.025	$10^6/10^7$

The onset of significant matrix failure is approximately determined in terms of a crack initiation stress $\hat{\sigma}$ and crack initiation strain $\hat{\varepsilon}$ as shown in the overall stress-strain diagram in Fig. 4. In the diagram, a linear elastic increase can be observed and a (local) stress maximum $\hat{\sigma}$ is reached at the strain $\hat{\varepsilon}$. At that point the formation of cracks in the matrix initiates and in the following the crack propogation leads to a stress release. It is noted that the damage onset is similar to the predictions in [63], despite the limited comparability, e.g., due to different roving volume fractions. Only when the cracks fully traverse the sample the stress increases again. For a maximum resistance to cracking it is therefore interesting to find material and geometry parameters that maximize $\hat{\sigma}$ and $\hat{\varepsilon}$.

First, the influence of the roving vertical and lateral dimensions, i.e., the thickness and the width, on $\hat{\sigma}$ and $\hat{\varepsilon}$ was investigated. The results are depicted in Fig. 5. With increasing thickness of the roving a decrease in the overall stiffness $\sigma_{xx}/\varepsilon_{xx}$ in the linear-elastic regime and a decrease in the crack initiation stress $\hat{\sigma}$ are obtained. This may be explained by the fact that the undeformed

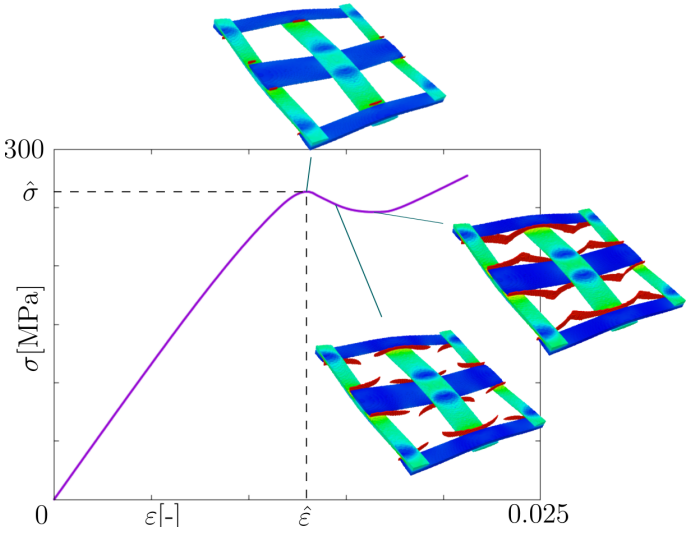

Fig. 4. Stress strain diagram for uniaxial tension test. For the strain $\varepsilon = \hat{\varepsilon}$ cracking in the matrix initially starts and the stress reaches a maximum $\hat{\sigma}$.

thicker rovings exhibit a rather undulated shape, while the thinner ones have an almost flat appearance. It is therefore not surprising that the flatter rovings are better qualified to carry macroscopically applied tensile stresses, since they are less prone to elongate under tensile loads and thus alleviate the matrix material in comparison to the more undulated thicker rovings. The results for the crack initiation strain $\hat{\varepsilon}$ are inconclusive. The dimensions (in mm) of the thinnest structure depicted in the figure are $1 \times 1 \times 0.0625$ and the major and minor half axes of the rovings' elliptic cross section are 0.2 mm and 0.0125 mm, respectively. It should be mentioned that the simulation of the thinnest structure in Fig. 5a was carried out with the material parameter l taking the value $l = 0.0125$ mm, since otherwise the crack width would have been clearly larger than the vertical distance between the rovings. Decreasing l is known to increase the overall stress for crack initiation in certain situations, which may explain the high value of $\hat{\sigma}$ at the thickness ratio of 1 in Fig. 5a. Nevertheless, the results indicate a possible advantage of vertically thinner rovings of the compound material. This finding could be correlated to the conclusion drawn by [65] who conducted a numerical and experimental analysis of the elastic behavior of plain weave fabric lamina. In particular, the effect of the undulation and lamina thickness on the in-plane elastic constants of E-glass/epoxy and T-300 carbon/epoxy has been investigated, and it has been shown that the increase of the lamina thickness results in a decrease of the elastic modulus of the overall composite which supports the observation illustrated in Fig. 5.

(a) Influence of thickness

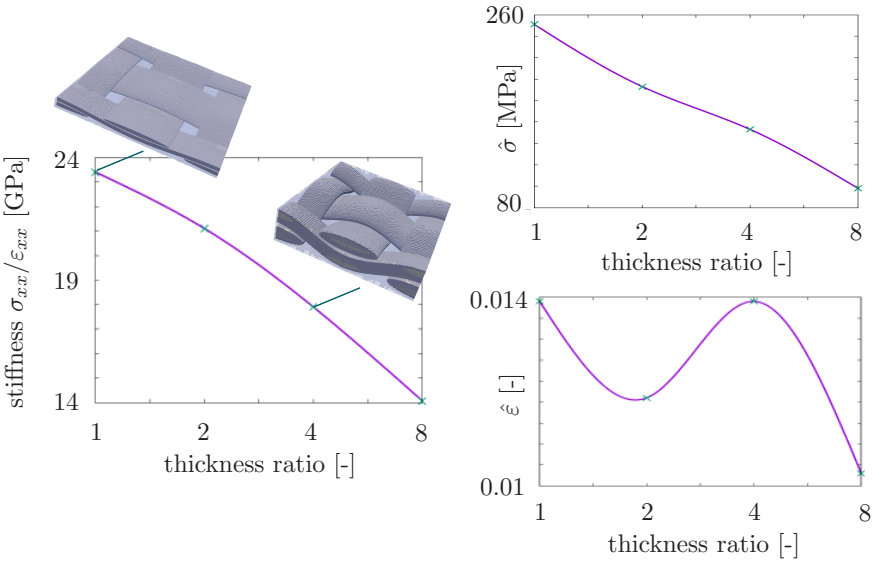

(b) Influence of width

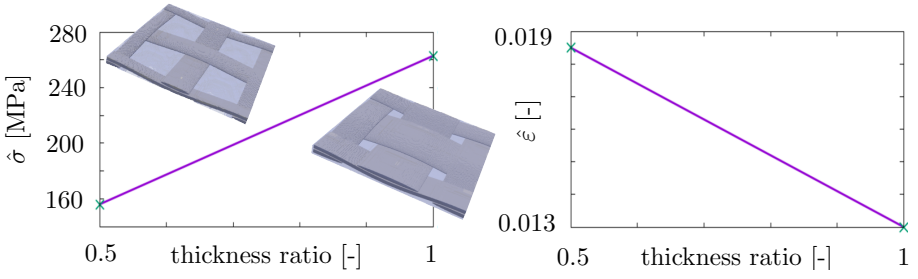

FIG. 5. (a) Influence of roving thickness on the stiffness $\sigma_{xx}/\varepsilon_{xx}$ in the linear-elastic regime and crack initiation stress $\hat{\sigma}$ and strain $\hat{\varepsilon}$ and (b) influence of roving width on $\hat{\sigma}$ and $\hat{\varepsilon}$. The actual data points are indicated by the crosses.

Next, the influence of the roving width on $\hat{\sigma}$ and $\hat{\varepsilon}$ was investigated. Here, the thicker structure (thickness ratio 1) is identical to the thinnest one from the thickness comparison (thickness ratio 1). However, the matrix is slightly softer ($\lambda_{\mathrm{M}} = 2592.6$ MPa) in order to investigate the stiffness' influence. The results (see Fig. 5b) show a width increase by a factor of 2, an increase in $\hat{\sigma}$ in the order of 100MPa but a decrease in $\hat{\varepsilon}$ by almost one third. As the rovings are stiffer than the matrix, the macroscopically applied strain tends to localize more in the matrix than in the rovings. For rovings with decreased width, the matrix volume fraction increases and thus there is more matrix material available for the aforementioned localization of the macroscopic strain. As a result, the overall composite can endure higher strain values.

Finally, the influence of Young's modulus of the roving material E_{R} and the elastic energy release rate $g_{\mathrm{c}}^{\mathrm{e}}$ of the matrix material on the cracking resistance was investigated. The results are depicted in Fig. 6. A higher value of Young's modulus of the rovings leads to an increase in $\hat{\sigma}$ and a decrease in $\hat{\varepsilon}$. In case of an increased matrix elastic energy release rate both $\hat{\sigma}$ and $\hat{\varepsilon}$ are also increased.

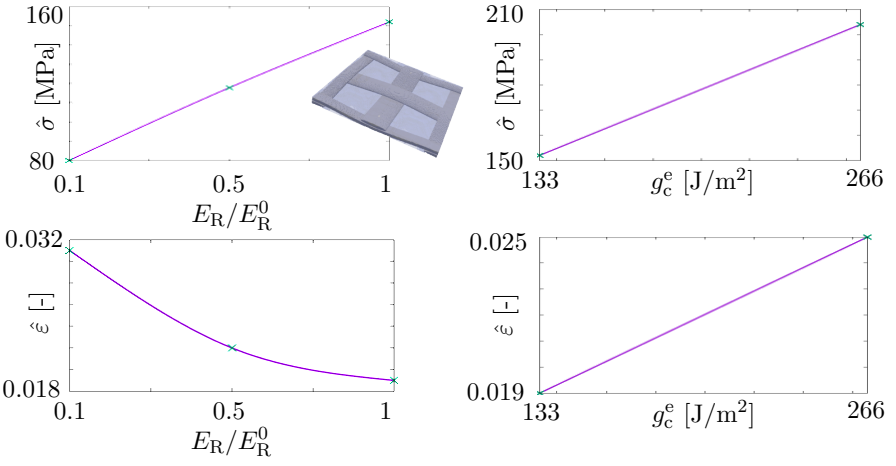

FIG. 6. Influence of Young's modulus E of roving material and elastic energy release rate $g_{\mathrm{c}}^{\mathrm{e}}$ of matrix material on crack initiation stress $\hat{\sigma}$ and strain $\hat{\varepsilon}$ with $E_{\mathrm{R}}^0 = 47.49\,\mathrm{GPa}$ and $\nu_{\mathrm{R}} = 0.25$.

5.2. Application of the model to the core-shell rubber nano-particles reinforced epoxy

A comparison between the tensile responses of a microscopic computational unit cell including voids with different volume fractions and different sizes has been carried out to investigate the effect of these micro-structural parameters on the tensile behavior of the CSR particles modified epoxy. One can show that the applied boundary conditions[7] are consistent with the Hill–Mandel condition. The effective value of Young's modulus was obtained from the quotient $E = \sigma_{xx}/\varepsilon_{xx}$ in the initial linear-elastic regime. Other numerical tensile tests considering different matrix properties and using the same unit cell (see Fig. 1a) also have

[7]Here, the boundary conditions applied to the unit cell in Fig. 1a were such that the displacements in the tensile direction ($\hat{=}x$-direction) on two opposed faces. The displacements in the lateral directions on these faces were free ($\hat{=}$zero-traction Neumann-type boundary conditions). On the lateral faces (i.e., the remaining four faces), zero-traction boundary conditions were applied.

been performed to check if this variation could improve the performance of such composites. If not mentioned otherwise, the (isotropic) material properties in Table 1 are applied.

5.2.1. Particle volume fraction effect. To investigate the effect of the particle volume fraction on the mechanical properties of the modified matrix, spherical voids with 50 nm radius were included in a cube with dimensions 0.5 μm × 0.5 μm × 0.5 μm in an ordered arrangement as shown in Fig. 1a.

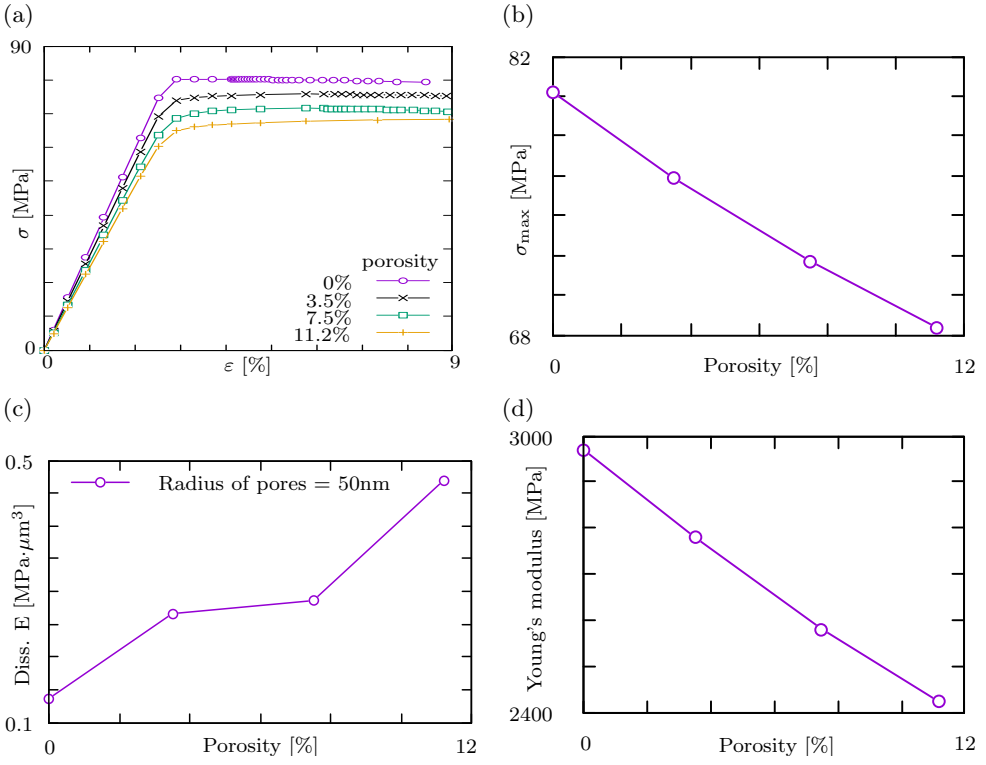

FIG. 7. Effect of particle volume fraction (uniaxial loading) on (a) stress-strain responses, (b) maximum strength, (c) amount of dissipated energy due to plastic deformation and (d) stiffness. Here, 'porosity' denotes the particle volume fraction in %.

As mentioned before, the CSR-particles are modelled as voids, as particle cavitation typically occurs in the overall elastic region and its influence on the effective response is assumed small (see [66]). This approach may be enhanced in the future by including cavitation criteria. Such a criterion is proposed, e.g., in the numerical model in [67], which includes plasticity but no damage variable. For different volume fractions between 0% and 11%, the corresponding stress-strain relations, tensile strength $\sigma_{\max}$, stiffness E and dissipated energy are depicted in

Fig. 7a to 7d, respectively. With increasing volume fractions the tensile strength and stiffness decrease as shown in Figs. 7b and 7d. It is noted that the data in Fig. 7b is in reasonable agreement with the experimental data reported in [62].

As explained above, the matrix material in the vicinity of the voids experiences high stresses during the loading of the whole volume and their growth makes the micro-structure absorb more energy before failure. Furthermore, as shown in Fig. 7c the amount of dissipated energy at the stress maximum increases with increasing number of particles. A larger dissipation means that the material absorbs more energy when being plastically deformed and thus indicates a larger toughness of the material. This is interpreted as follows. For 0% particles (being modelled as voids), the material and elastoplastic deformation are homogeneous. For a small volume fraction of voids, the strains in the initial stage of the process are mainly localized in the vicinity of the growing voids, where a significant amount of deformation energy is absorbed. The overall composite thus absorbs more energy than a homogeneous matrix material due to the inhomogeneous microscopic deformation field. This effect can be intensified by increasing the initial volume fraction of the particles/voids. With ongoing deformations the voids grow and deformation fields around the voids start to interact until, finally, the voids coalesce. For larger initial void volume fractions, the coalescence stage happens earlier. If the initial void volume fraction is too large, coalescence happens soon after the onset of inelastic deformations, i.e., the material is unable to absorb significant amounts of energy.

5.2.2. Particle size effect. For the investigation of nano-particle size effects on the modified matrix behavior, different volume fractions for particles with 25 nm and 50 nm radius were compared.

The resulting stress-strain diagrams for the 25 nm particles and the comparison of dissipated energy for both sizes are given, respectively, in Figs. 8a and 8b. Similar effects as before can be seen with this model as well.

In summary, the results show a clear trend that an increase of the particle volume fraction may improve the energy absorption capability of the material. The curves also give a first quantitative impression of this effect, although further research will be necessary in the future to investigate the influence of the unit cell size, which is beyond the scope of this work.

5.2.3. Epoxy properties effect. The effect of initial yield stress σ_{y0} and elastic energy release rate g_c^e on the compound behavior was investigated by tensile tests with a volume fraction of 8% and particle size 25 nm. The corresponding stress-strain diagrams are given in Fig. 9.

As expected, Fig. 9a shows that a lower yield strength results in an earlier onset of plastic deformation. Therefore, up to certain load level, the dissi-

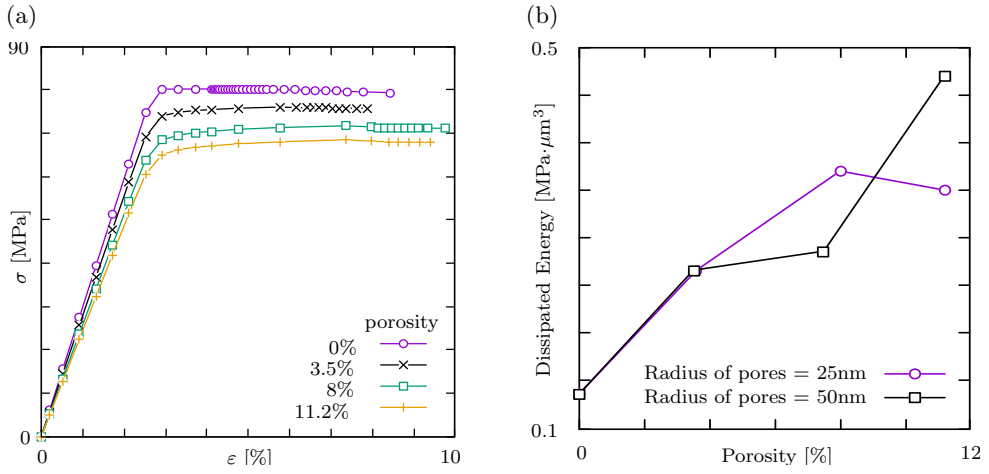

FIG. 8. Effect of particle size: (a) Stress-strain response for different volume fractions of voids with radius 25 nm included in a 0.5 μm × 0.5 μm × 0.5 μm cubic unit cell and (b) comparison of dissipated energy for 25 nm and 50nm particle size.

pated inelastic energy is greater with lower yield strength. However, at the stress maximum, the inelastic energy consumed is more important with higher yield strength. The effect of the variation of the elastic energy release rate of the epoxy on the behavior of the material is illustrated in Fig. 9b. Indeed, up to the fracture, the different compounds with different values of g_c^e show the same behavior as well as the same dissipation of inelastic energy. This can be explained by the fact that g_c^e is a fracture property while the initial deformation stage is entirely plasticity-dominated and the damage does not play a role initially.

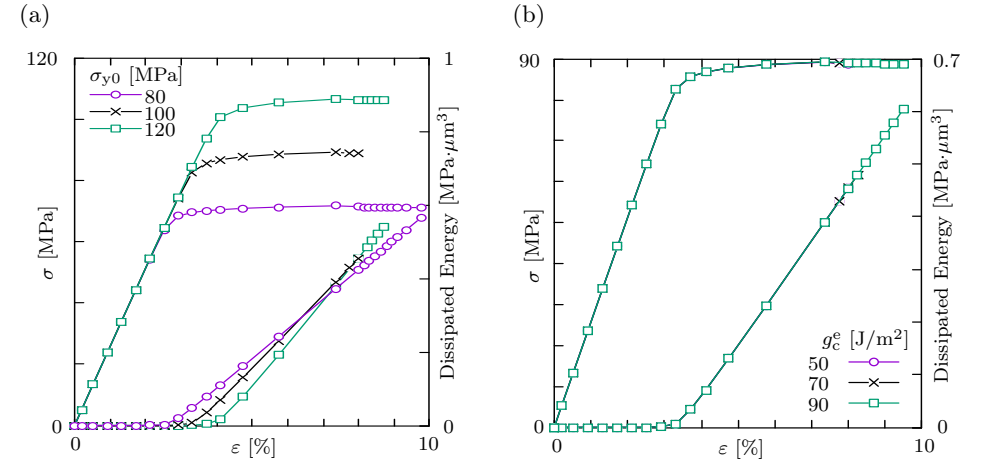

FIG. 9. Stress-strain response and amount of dissipated energy for different (a) initial yield stresses σ_{y0} and (b) elastic energy release rates g_c^e.

5.3. Application of the model to unidirectional carbon fibers reinforced epoxy

5.3.1. Material properties calculation. To calculate the properties of the whole composite a campaign of numerical tests such as longitudinal, transversal, and in-plane[8] shear tensile tests have been conducted. For this purpose, the unit cell (Fig. 1b) of the composite, assumed perfect without defects (voids) has been used. For the unidirectional fiber reinforced epoxy, additional material parameters are needed to describe the anisotropic response of the fibers. These are listed in Table 2, assuming the fibers to be transverally isotropic. As the fibers are assumed to stay elastic (fiber fracture is not considered), no anisotropic inelastic material properties are considered. Figure 10 outlines the deformation resulting from each loading at a maximum scale. Table 5 lists the calculated properties of the overall composite[9].

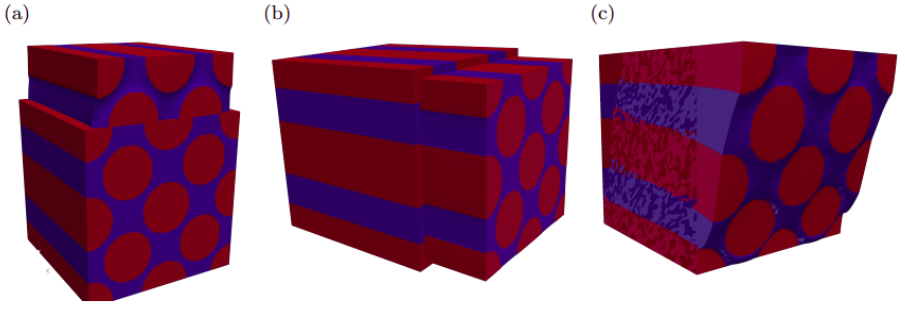

FIG. 10. Composite cell under (a) transverse loading, (b) longitudinal loading and (c) in-plane shear loading.

Table 5. Calculated effective elastic and strength-related properties of the CFRP composite.

Longitudinal Young's modulus	143480 MPa
Transverse Young's modulus	6687 MPa
Shear modulus	3640 MPa
Transverse strength	97.9 MPa
In-plane shear strength	52 MPa
Poisson's ratio	0.28

[8]Since macroscopic realizations of the microstructure considered here are usually plies, the term "in-plane" refers to the plane of a ply.

[9]The values of Young's moduli in longitudinal and transverse direction in Table 5 related to Fig. 10a and 10b, respectively, were obtained using boundary conditions in analogy to Section 5.2. The boundary conditions for the shear test in Fig. 10c were such that the displacement vectors on the top and bottom faces were fully prescribed and symmetry conditions were used on the left and on the right faces.

5.3.2. Fiber volume ratio effect. In this section, the micro-structure is randomized based on the fraction of fiber reinforcement. Typically, a higher fiber volume fraction results in better mechanical properties of the composite. However, it has been demonstrated that an increase in fiber content would not always, as one would normally think, improve the energy-absorption capability of a CFRP material [68]. The accuracy of this observation has been assessed in the case of our material by the calculation of the energy absorbed up to the stress maximum level by the material subjected to transverse loading for two fiber volume fractions (50% and 60%). The behavior of the material being subjected to longitudinal, transverse, and plane shear loading is illustrated in Fig. 11. Within the

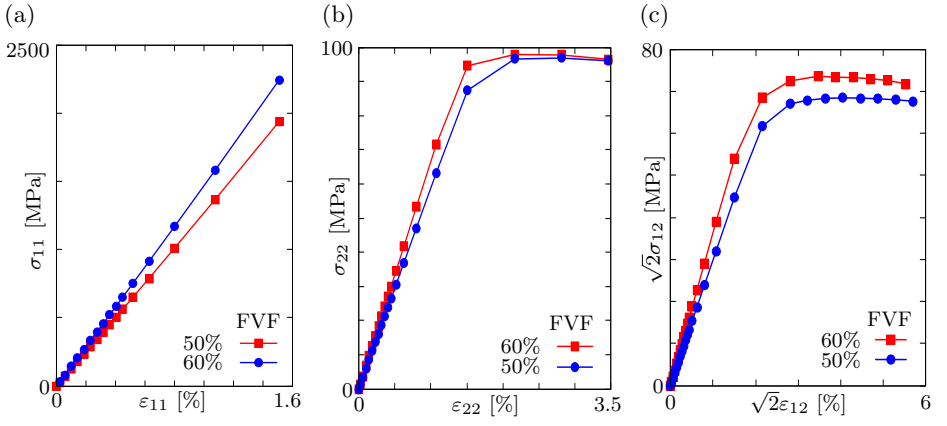

FIG. 11. Fiber volume ratio effect on (a) longitudinal behaviour, (b) transverse behavior and (c) in-plane shear behaviour.

simulated region, the results for 60% fiber volume fraction (FVF) in Fig. 11c are similar to the strength reported in [69], where the shear properties of a composite

Table 6. Fiber volume fraction (FVF) effect on mechanical properties of the CFRP composite, where '1' denotes the direction of the fibers. The absorbed energy is the total work generated on the composite minus the elastic energy.

	FVF = 50%	FVF = 60%
E_{11} [MPa]	126400	143480
E_{22} [MPa]	5920	6687
G_{12} [MPa]	2980	3630
$\sigma_{22,\max}$ [MPa]	96.87	97.9
$\sqrt{2}\sigma_{12,\max}$ [MPa]	68.43	73.58
ν_{12}	0.257	0.246
Absorbed energy density 22 [MPa]	1.00	0.63
Absorbed energy density 12 [MPa]	0.75	0.64

with 59% FVF were investigated. At first glance, one could assume that higher fiber volume fractions generally lead to improved material properties. However, it can be drawn from Table 6 that this is true only in terms of strength and stiffness, whereas the variation of the fiber volume fraction showed an unexpected effect on the capability of the material to absorb energy. Indeed, the calculation revealed that a CFRP with only 50% of fibers absorbs more energy than the one with 60%.

Therefore, we can confirm through our numerical study that an increase in the fiber content does not necessarily improve the energy absorption capability indicative of the composite material toughness. A possible explanation for this finding is that as the fiber volume fraction increases, the volume of the matrix between the fibers decreases. This further leads to a decrease in the transverse strength of the composite which is a matrix dominated strength. As the transverse strength decreases, matrix cracks form at lower strains, resulting in an early failure and a reduction in the amount of the energy absorbed. This assertion could be backed up by Fig. 12 which shows the damage distribution throughout the unit cell at an early level of transverse loading for both volume fractions of fibers 50% (diameter of fibers = 6.5 μm) and 60% (diameter of fibers = 7 μm). Indeed, from this figure, one could easily notice that at the same level of loading (low) the material with a fiber volume fraction of 60% exhibits a higher intensity of damage in the matrix. This high intensity of damage reflects the early creation of matrix cracks being at the origin of the low toughness (or also called energy absorption capability) found for this material combination.

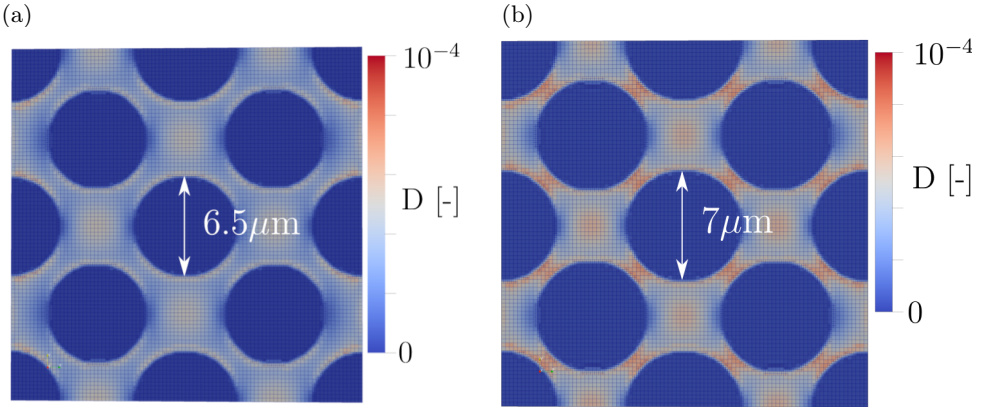

Fig. 12. Fiber fraction effect: damage distribution in the composite cell under low traverse loading for (a) FVF = 50% and (b) FVF = 60%.

5.3.3. Fiber shape effect. In addition to typical fibers with circular cross sections, another type of fibers with non-circular cross sections (or also called elliptical

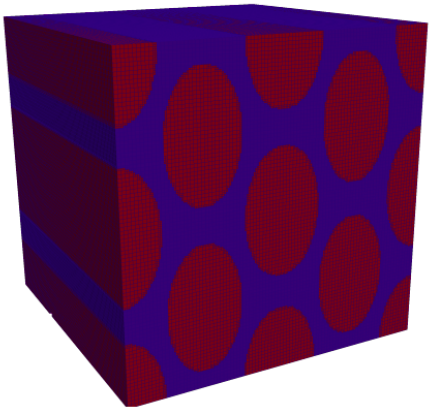

FIG. 13. Cell of the composite reinforced by 60% of elliptical fibers.

fibers) has been considered. The unit cell of such combination is shown in Fig. 13. Here, voids are not modeled and the typical fraction of fibers of 60% is considered.

A comparison between the responses obtained for the application of longitudinal, transverse and in plane shear loadings to two different unit cells of composites reinforced by 60% of elliptical and circular fibers has been performed. This comparison is illustrated in Fig. 14.

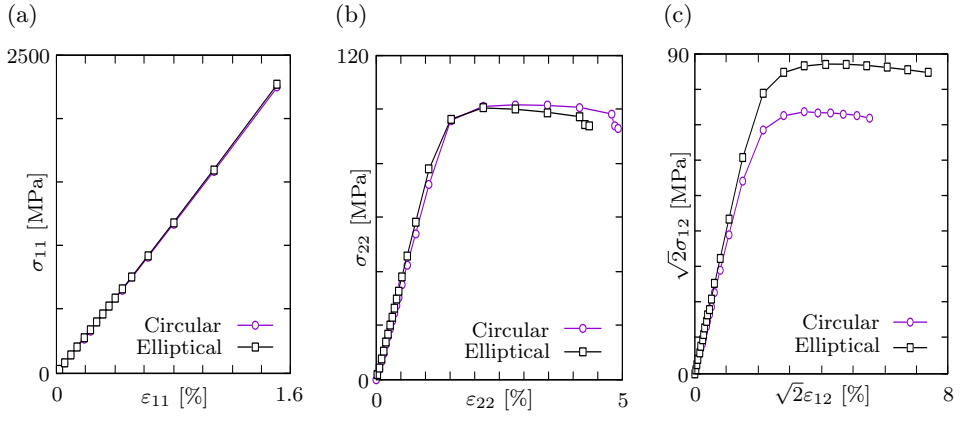

FIG. 14. Fiber shape effect on (a) longitudinal behavior, (b) traverse behavior and (c) in-plane shear behavior.

The figure shows that the alteration from circular to elliptical fibers has a mild enhancement effect on the longitudinal and the transverse behavior of the overall material. However, a significant enhancement in terms of in-plane shear properties could be granted to this alteration. The enhancement caused by

the introduction of elliptical fibers instead of circular fibers does not cover only the stiffness and the strength but also the energy absorption capability. Indeed the energy absorbed by the material up to the maximum transverse strength is enhanced by 61% in the case of in plane shear loading. This result could be supported by the study [70], where it was found out that elliptical cross-sections of the carbon fibers have a lower tendency to form transverse cracks compared to circular cross-section carbon fibers. Table 7 collects the values of all parameters calculated through this investigation.

Table 7. Fiber shape effect on mechanical properties of the CFRP composite, where '1' denotes the direction of the fibers.

	Elliptical fibers	Circular fibers
E_{11} [MPa]	145400	143480
E_{22} [MPa]	7300	6687
G_{12} [MPa]	4049	3630
$\sigma_{22,\max}$ [MPa]	100.4	97.9
$\sqrt{2}\sigma_{12,\max}$ [MPa]	87	73.58
ν_{12}	0.2544	0.246
Absorbed energy density 22 [MPa]	0.7	0.63
Absorbed energy density 12 [MPa]	1.03	0.64

5.3.4. Matrix voids effect. Most studies in the literature correlate the degradation of mechanical properties with the void content increase and do not take into account other void parameters such as size, shape, and spatial distribution. The review [71] lists all these studies and also other studies that emphasized the relevant effect of parameters other than the voids amount on the mechanical performance of the fiber-reinforced composites. In this section, results obtained through the investigation of the voids' effect on the transverse behavior of the carbon fiber-reinforced epoxy is presented and analyzed. The fiber fraction considered in this part of our study is also 60%, however in order to simplify the problem and to save time, the unit cell considered here is not a cube but a plate with a thin thickness. Indeed, the incorporation of the voids implies more refinement and then longer time of simulation. The voids modeled in this study represent matrix defects whose considerable effect can only be noticed in the transverse behavior. Therefore only a transverse tensile test has been simulated to carry out this investigation. Prior to the variation of the voids' parameters and the assessment of the effect of this variation on the material properties, we illustrate through Fig. 15 a general overview of the effect of such defects on the failure behavior of the material. It could be easily noticed that the presence of the voids even with a small fraction (0.2%) could affect the cracks formation and distribution throughout the material.

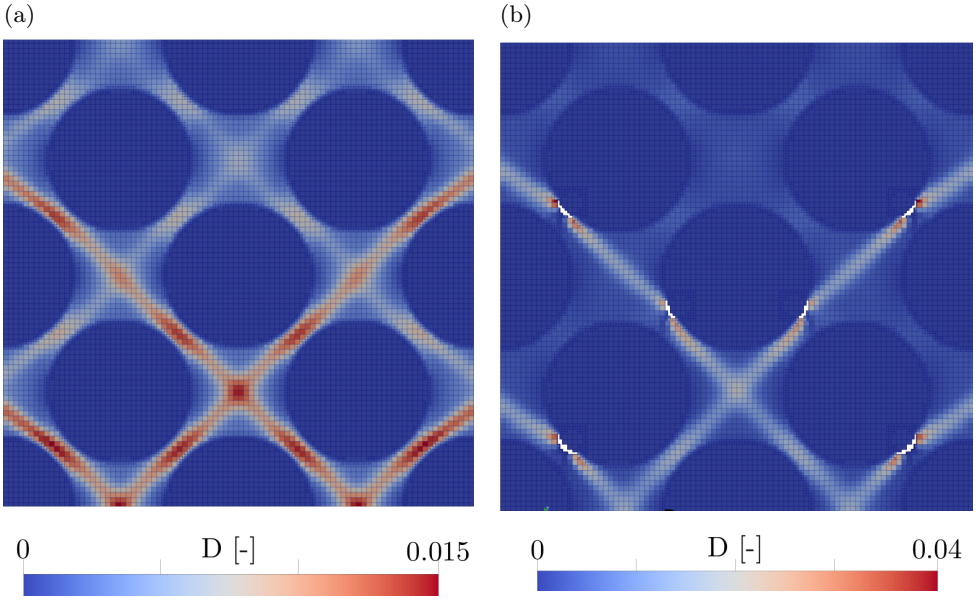

FIG. 15. Damage distribution at the same loading level in the CFRP (a) without voids and (b) with voids.

Porosity effect. To investigate the effect of the porosity[10] amount, 5 volume fractions have been considered in addition: 2%, 4%, 8%, 10% and 14%. Results obtained from this investigation are presented in Fig. 16.

As expected, the incorporation of the voids in the CFRP material caused a dramatic decline in the transverse strength and stiffness. For instance, 4% of the increase in the voids content caused a reduction of 25% for σ_{22} and 18% for E_{22}. However, what was not expected is the result shown in Fig. 16c. Indeed, the energy absorption capability of the material is improved up to 8% of voids content. This same observation has been made in several experimental studies [71]. And the physical explanation suggested for this unexpected finding is that around these voids new plastic zones are formed allowing for an extra energy-absorption. Though, it should be noted that this enhancement is granted to a specific reduced fraction of porosity which is estimated according to our investigation to be 8%. Based on these findings, a matrix porosity of up to 8% in the carbon fibers reinforced epoxies leads to an enhancement in the energy absorption capability, but implies a decrease in transverse stiffness and strength.

Voids distribution effect. To investigate the effect of the distribution of the voids on the transverse behavior of the material, 2% of void volume fraction has

[10]Here, the porosity describes the volume ratio (in %) of pores in the material, usually representing manufacturing defects.

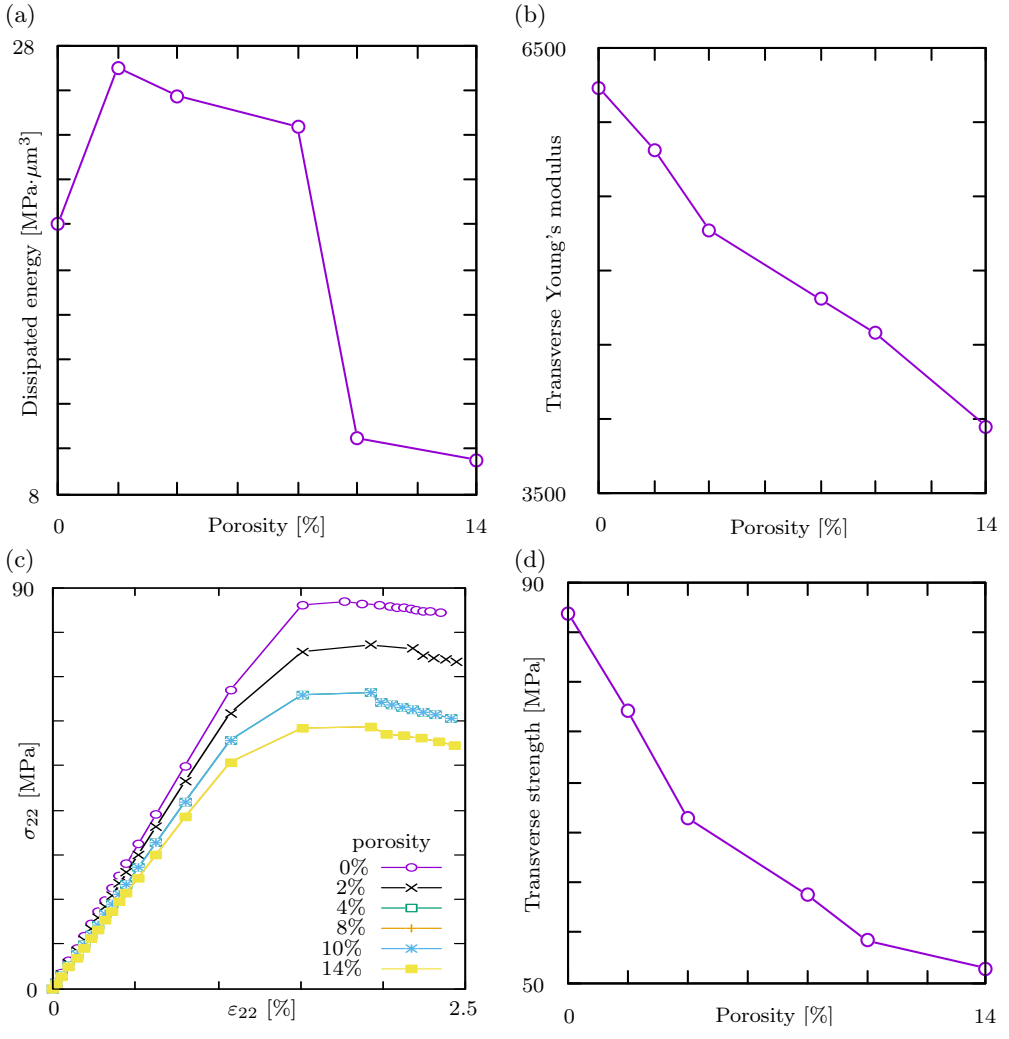

FIG. 16. Effect of particle volume fraction on the (a) stress-strain responses under uniaxial loading, (b) maximum strength, (c) amount of dissipated energy due to plastic deformation and (d) stiffness.

been considered. This amount of porosity has been represented by 4 voids of a diameter equal to 1.5 μm. Figure 17 shows two kinds of pores arrangement. In the first one, the 2% of porosity is concentrated and in the other one, it is well distributed. This investigation shows that the accumulation of voids results in a slight gain in terms of transverse stiffness and transverse strength (respectively +3.6% and +1.3%) against a significant loss in terms of deformation and energy absorption capability (respectively −21% and −66%). Corresponding calculated values are shown in Table 8.

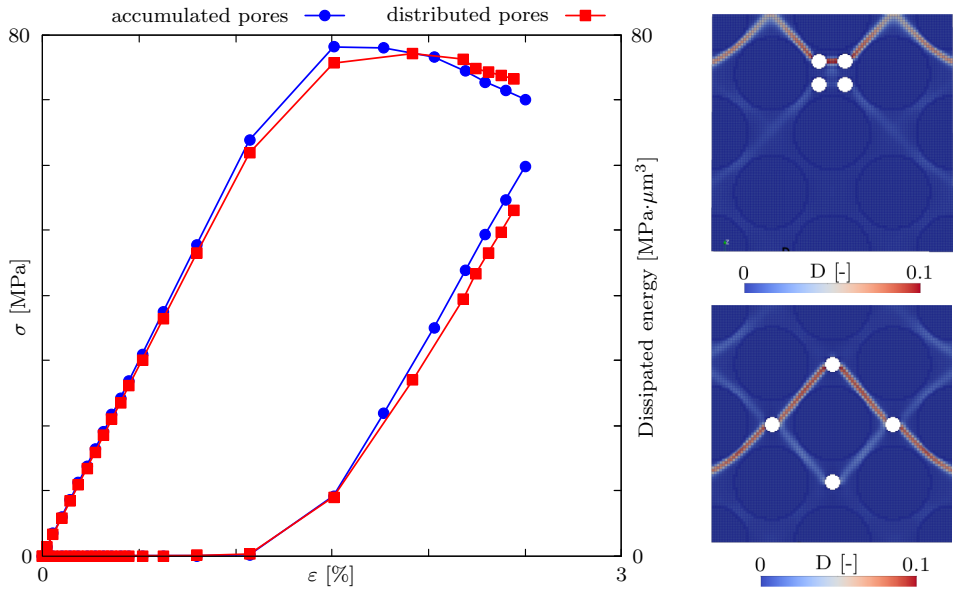

FIG. 17. Voids distribution effect on the transverse behavior of the CFRP material.

Table 8. Effect on the arrangement of the defects on transverse properties of the CFRP composite.

	Distributed	Accumulated
Porosity [%]	2	2
Diameter [μm]	1	1
E_{22} [MPa]	5812	6041
$\sigma_{22,\max}$ [MPa]	77.1	78.1
Absorbed energy 22 [MPa · μm^3]	26.97	9.18

6. Conclusions

Microscopic failure mechanisms were investigated by finite element simulations using a combination of geometrically nonlinear isotropic elastoplasticity and an isotropic damage model with gradient-extension. Simulations made use of a variational constitutive update algorithm based on the exponential map and an adaptive meshing algorithm for a refined numerical resolution of the cracked regions.

Three composite microstructures were simulated and numerically characterized: core-shell rubber particles reinforced-epoxy, woven glass fiber-reinforced epoxy, and carbon fiber-reinforced epoxy. The study consisted in the investiga-

tion of the effect of the microstructural parameters variation on the behavior of the model. For the woven roving-reinforced composite, it was demonstrated that reduced thicknesses of the rovings were beneficial for the resistance against crack initiation. Reducing the width, however, increases the load carrying capability in terms of tensile strains but has the opposite effect in terms of tensile stresses.

For the core-shell rubber particles reinforced composite, the influence of particle volume fraction, particle size, and matrix material properties on the overall material properties was tested on a 3-dimensional cubic model representing a unit cell of the matrix including spherical voids representative of cavitated reinforcing particles. Here, stiffness and strength of the composite were decreased with increasing the volume fraction of the particles, while the amount of dissipated energy tended to increase. The matrix properties, such as the energy release rate and the yield stress, have been also considered amongst the microstructural parameters whose variation could enhance or impair the performance of the core-shell-rubber particles modified epoxy. It has been found that the energy release rate initially has no effect on the properties of the material while the increase of the yield stress leads to an increase of the material strength and energy absorption capability.

The investigation of the microstructural variability effect on the behavior of carbon fiber-reinforced epoxy included the consideration of several parameters relating to both components, fibers and matrix. Indeed, two cross-section shapes (circular and elliptical) have been considered in the unit cell specific to this composite and two volume fractions of fibers (50% and 60%) have been tested. Matrix defects being a decisive factor in the assessment of the behavior of the composite, have been carefully studied. These defects were depicted by spherical voids with different volume fractions, different diameters and different arrangements.

The first key finding from this investigation is that fibers with elliptical cross section are better reinforcing agents than fibers whose cross section shape is circular. A further interesting finding is that CFRP with 50% of fibers has a better energy absorption capability than CFRP with 60%. However a decrease in the fibers amount would lead to a decrease in the stiffness and the strength of the overall composite.

Results obtained from the simulation of the tensile response of the composite unit cell including voids have been unexpected. Indeed, it has been found that voids up to a specific volume fraction could improve the energy absorption capability, while the strength and stiffness decrease. Results obtained from multivariate analyses relating to both materials (carbon fiber-reinforced epoxy and core-shell rubber particles reinforced epoxy) have been gathered respectively in Appendix A and Tables 9–12.

Appendix A. Summary of major results

In Table 9, the effects of different microstructural parameter modifications on the investigated overall properties of the core-shell rubber particles modified

Table 9. Microstructural variability effect on the properties of the core-shell rubber particle modified epoxy , particle volume fraction (p.v.f.) in %.

Parameter	Variation	Effect on:		
		Young's modulus	tensile strength	absorbed energy
p.f.v., radius	3.5% 50 nm	−6.4%	−5.36%	+95.2%
	7.5% 50 nm	−13.1%	−10.6%	+109.8%
	11.2% 50 nm	−18.45%	−14.8%	+244%
	3.6% 25 nm	−6.9%	−5.23%	+95.2%
	8% 25 nm	−13.9%	−10.6%	+171.5%
	11.2% 25 nm	−18.5%	−14.7%	+156.8%
Yield stress of matrix	100 MPa	0%	+24.4%	+5.4%
$r = 25$ nm, p.f.v: 8%	120 MPa	0%	+48.6%	+2.7%
Energy release rate	70 J/m^2	0%	0%	0%
of the matrix	90 J/m^2	0%	0%	0%
$r = 25$ nm, p.f.v: 8%				

Table 10. Material properties of the unmodified epoxy matrix of the core-shell rubber reinforced composite.

Young's modulus E [MPa]	Initial yield stress σ_{y0} [MPa]	Elastic energy release rate g_c^e [J/m^2]	Absorbed energy [MPa·μm^3]
2970	80.2	50	0.1363

Table 11. Micro-structural variability effect on the properties of the carbon fiber-reinforced epoxy.

Parameter	Variation						Absorbed energy	
		E_{11}	E_{22}	G_{12}	σ_{22}	$\sqrt{2}\sigma_{12}$	Trans.	In-plane
Shape of fibers	Elliptic	+1.3%	+9%	+11.5%	+2.5%	+18%	+11%	+61%
Fiber volume fraction	50 %	+11.9%	−11.5%	−17.9%	−1%	−7%	+58.7%	+17.2%
Porosity	2%		−6.7%		−11.3%		+35%	
	4%		−15.6%		−23.6%		+28.7%	
	8%		−22.5%		−32.4%		+21.9%	
	10%		−26.2%		−37.7%		+47.6%	
	14%		−36.3%		−40.8%		+52.5%	
Voids diameter	1μm		−6.7%		−11.3%		+35%	
	1.5μm		−7.3%		−13.3%		+16.5%	
Voids distribution	distributed		−6.7%		−11.3%		+35%	
	accumulated		−3%		−10.1%		−54.1%	

epoxy are summarized. Values representing the reference of comparison correspond to the properties of the CSR/epoxy material without voids (porosity = 0%) subjected to the same loading conditions. These values are presented in Table 10.

Table 11 is the analogon of Table 9 for the carbon fiber reinforced epoxy. Values representing the reference of comparison correspond to the properties of the CFRP material without voids (porosity=0%) subjected to the same loading conditions. These values are presented in Table 12.

Table 12. Material properties of the typical carbon fiber-reinforced composite without defects.

Cross section shape of fibers	circular
Volume fractions of fibers	60%
Longitudinal Young's modulus	143480 MPa
Transverse Young's modulus	6687 MPa
Shear modulus	3640 MPa
Transverse strength	97.9 MPa
Absorbed energy under transverse loading	0.63 Jμm
Absorbed energy under in-plane loading	0.64 Jμm

Appendix B. Proof of coaxiality of $\mathbf{b}^{\mathrm{p}}$ and $\mathbf{R}^{\mathrm{e}\top}\mathbf{b}^{\mathrm{e}}\mathbf{R}^{\mathrm{e}}$

The spectral decomposition of the inverse of $\mathbf{c}^{\mathrm{p}}$ and the related incompressibility constraint (see Eqs. (2.12)) read

$$\mathbf{c}^{\mathrm{p}-1} = \sum_{i=1}^{3} c_i^{\mathrm{p}-1}\mathbf{N}_i \otimes \mathbf{N}_i, \qquad c_1^{\mathrm{p}-1}c_2^{\mathrm{p}-1}c_3^{\mathrm{p}-1} = 1. \tag{B.1}$$

The variation of the potential $\pi_{\vartriangle}$ with respect to $\mathbf{c}^{\mathrm{p}-1}$ is given by

$$\delta\pi_{\vartriangle} = g(D)\frac{\partial\psi_{\mathrm{e}}}{\partial\mathbf{b}^{\mathrm{e}}} : (\mathbf{F}^{\mathrm{etr}}\delta\mathbf{c}^{\mathrm{p}-1}\mathbf{F}^{\mathrm{etr}\top}), \tag{B.2}$$

where we assume that exclusively the triad $\{\mathbf{N}_1, \mathbf{N}_2, \mathbf{N}_3\}$ is varied, since we seek its optimal orientation such that $\delta\pi_{\vartriangle} = 0$. This condition implies that $\mathbf{c}^{\mathrm{p}-1}$ is coaxial with

$$2\mathbf{F}^{\mathrm{etr}\top}\frac{\partial\psi_{\mathrm{e}}}{\partial\mathbf{b}^{\mathrm{e}}}\mathbf{F}^{\mathrm{etr}} = 2\mathbf{f}^{\mathrm{p}\top}\mathbf{R}^{\mathrm{e}\top}\left(\mathbf{b}^{\mathrm{e}}\frac{\partial\psi_{\mathrm{e}}}{\partial\mathbf{b}^{\mathrm{e}}}\right)\mathbf{R}^{\mathrm{e}}\mathbf{f}^{\mathrm{p}} = \mathbf{u}^{\mathrm{p}}\mathbf{r}^{\mathrm{p}\top}\mathbf{R}^{\mathrm{e}\top}\boldsymbol{\tau}\mathbf{R}^{\mathrm{e}}\mathbf{r}^{\mathrm{p}}\mathbf{u}^{\mathrm{p}}, \tag{B.3}$$

where $\boldsymbol{\tau}$ is coaxial with $\mathbf{b}^{\mathrm{e}}$. Based on this result, it is trivial to show that $\mathbf{b}^{\mathrm{p}}$ and $\mathbf{R}^{\mathrm{e}\top}\mathbf{b}^{\mathrm{e}}\mathbf{R}^{\mathrm{e}}$ are coaxial using Eq. (2.12).

Appendix C. Algorithmic tangent operators

Due to the potential structure, the algorithmic tangent operators are completely symmetric and involve the linearization of the following terms of the weak form (Eqs. (2.17) and (2.18))

$$\boldsymbol{\tau} : \boldsymbol{d}_\delta, \qquad \frac{\partial \pi_\Delta}{\partial D}\delta D, \qquad \frac{\partial \pi_\Delta}{\partial \mathrm{Grad}(D)} \cdot \mathrm{Grad}(\delta D). \tag{C.1}$$

Since the linearization of the latter two terms and the computation of $\partial\boldsymbol{\tau}/\partial D$ is rather trivial, we restrict ourselves to the linearization of the more complex first expression, which (for fixed D) can be rearranged to yield the well-known relation

$$\Delta(\boldsymbol{\tau} : \boldsymbol{d}_\delta) = \mathrm{tr}(\mathbf{l}_\Delta \boldsymbol{\tau} \mathbf{l}_\delta^\top) + \mathbf{d}_\delta : \mathbf{c}^{\mathrm{a}} : \mathbf{d}_\Delta \tag{C.2}$$

with $\mathbf{l}_\Delta = (\partial \Delta\mathbf{x}/\partial \mathbf{X})\mathbf{F}^{-1}$ and $\mathbf{d}_\Delta = \mathbb{F}\mathbf{l}_\Delta$ and

$$\mathbf{c}^{\mathrm{a}} : \mathbf{d}_\Delta = \mathbf{F}^{\mathrm{etr}} \left(\frac{\partial \overline{\mathbf{S}}}{\partial \mathbf{C}^{\mathrm{etr}}} : \Delta \mathbf{C}^{\mathrm{etr}} \right) \mathbf{F}^{\mathrm{etr}\top}, \tag{C.3}$$

where $\Delta\mathbf{C}^{\mathrm{etr}} = 2\mathbf{F}^{\mathrm{etr}\top}\mathbf{d}_\Delta\mathbf{F}^{\mathrm{etr}}$ and the second Piola-Kirchhoff stress $\overline{\mathbf{S}} = \mathbf{F}^{\mathrm{etr}}\boldsymbol{\tau}\mathbf{F}^{\mathrm{etr}\top}$ with respect to the trial intermediate configuration is tacitly understood as a function of $\mathbf{C}^{\mathrm{etr}}$ and D. For the derivation, we follow lines analogous to SIMO [8], who discusses in detail how the algorithmic tangent related to a broad class of geometrically nonlinear time-discrete models can be expressed in terms of the related tangent of the small strain counterparts. We start by noting that in the plastic case, the yield criterion (see Eq. (2.28)) remains zero, if the input parameters ε and D are perturbed:

$$-\Delta f = \frac{\partial^2 \pi_\Delta}{\partial \Delta\gamma \partial \varepsilon} : \Delta\varepsilon + \frac{\partial^2 \pi}{\partial \Delta\gamma \partial D}\Delta D + \frac{\partial^2 \pi}{(\partial \Delta\gamma)^2}\Delta\gamma = 0. \tag{C.4}$$

For the small-strain counterpart of the geometrically nonlinear model, the linearization of the stress reads

$$\Delta\boldsymbol{\tau} = \frac{\partial \boldsymbol{\tau}}{\partial \varepsilon} : \Delta\varepsilon + \frac{\partial \boldsymbol{\tau}}{\partial D}\Delta D. \tag{C.5}$$

The algorithmic tangent operator $\tilde{\mathbf{c}}^{\mathrm{a}} = \partial\boldsymbol{\tau}/\partial\varepsilon$ can be derived from a straightforward linearization of Eq. (2.9) using Eq. (C.4):

$$\begin{aligned} \tilde{\mathbf{c}}^{\mathrm{a}} = {} & \big(g(D)H(\mathrm{tr}(\varepsilon)) + H(-\mathrm{tr}(\varepsilon))\big)\lambda \mathbf{I} \otimes \mathbf{I} \\ & + 2\mu g(D)\left(\mathbb{I}^{\mathrm{s}} - \frac{\Delta\gamma}{\|\varepsilon'\|}(\mathbb{P}' - \mathbf{n} \otimes \mathbf{n}) + \left(\frac{\partial^2 \pi_\Delta}{(\partial \Delta\gamma)^2} \right)^{-1} \mathbf{n} \otimes \frac{\partial^2 \pi_\Delta}{\partial \Delta\gamma \partial \varepsilon} \right), \end{aligned} \tag{C.6}$$

where $\mathbb{P}'$ is the deviatoric projector and $H(\bullet)$ is the Heaviside step function. Introducing the eigenvalues and eigenvectors $\overline{S}_i$ and $\overline{\mathbf{N}}_i$ of $\overline{\mathbf{S}}$ and $\overline{\lambda}_i$ and $\mathbf{n}_i$ as the eigenvalues and eigenvectors of $\mathbf{b}^{\mathrm{etr}}$, one can write (with $\mathbf{F}^{\mathrm{etr}}\overline{\mathbf{N}}_i = \overline{\lambda}_i\mathbf{n}_i$)

$$\boldsymbol{\tau} = \mathbf{F}^{\mathrm{etr}}\overline{\mathbf{S}}\mathbf{F}^{\mathrm{etr}\top} = \sum_{i=1}^{3} \overline{\lambda}_i^2 \overline{S}_i \mathbf{n}_i \otimes \mathbf{n}_i, \tag{C.7}$$

$$\mathbf{n}_i \otimes \mathbf{n}_i = \frac{(\mathbf{b}^{\mathrm{etr}} - \overline{\lambda}_j^2\mathbf{I})(\mathbf{b}^{\mathrm{etr}} - \overline{\lambda}_k^2\mathbf{I})}{(\overline{\lambda}_i^2 - \overline{\lambda}_j^2)(\overline{\lambda}_i^2 - \overline{\lambda}_k^2)}. \tag{C.8}$$

Further, we find that

$$\begin{aligned}\mathbf{F}^{\mathrm{etr}}\Delta\overline{\mathbf{S}}\mathbf{F}^{\mathrm{etr}\top} \\ = \sum_{i=1}^{3} \Big(\Delta\overline{S}_i \mathbf{F}^{\mathrm{etr}}(\overline{\mathbf{N}}_i \otimes \overline{\mathbf{N}}_i)\mathbf{F}^{\mathrm{etr}\top} + \overline{S}_i \mathbf{F}^{\mathrm{etr}}\Delta(\overline{\mathbf{N}}_i \otimes \overline{\mathbf{N}}_i)\mathbf{F}^{\mathrm{etr}\top}\Big).\end{aligned} \tag{C.9}$$

The linearization of $\overline{\mathbf{N}}_i$ and $\overline{\mathbf{S}}$ is given by:

$$\Delta\overline{\mathbf{N}}_i = \boldsymbol{\Omega}_\Delta \overline{\mathbf{N}}_i = \sum_{j=1}^{3} \Omega_{\Delta ji}\overline{\mathbf{N}}_j, \tag{C.10}$$

$$\Delta\overline{\mathbf{S}} = \sum_{i=1}^{3} \Delta\overline{S}_i \overline{\mathbf{N}}_i \otimes \overline{\mathbf{N}}_i + \overline{S}_i(\Delta\overline{\mathbf{N}}_i \otimes \overline{\mathbf{N}}_i + \overline{\mathbf{N}}_i \otimes \Delta\overline{\mathbf{N}}_i), \tag{C.11}$$

where it is exploited that $\Delta\mathbf{N}_i \cdot \mathbf{N}_i = 0$, such that the incremental rotation of the orthonormal eigenvectors can be expressed in terms of a skew-symmetric spin-like tensor $\boldsymbol{\Omega}_\Delta$. With this one can derive ($l \neq k$, no summation)

$$\begin{aligned}\overline{\mathbf{N}}_k \cdot \Delta\overline{\mathbf{S}}\,\overline{\mathbf{N}}_l &= \Delta\overline{\mathbf{N}}_k \cdot \overline{\mathbf{N}}_l\overline{S}_k + \overline{\mathbf{N}}_k \cdot \Delta\overline{\mathbf{N}}_l\overline{S}_l \\ &= \Omega_{\Delta lk}\overline{S}_k + \Omega_{\Delta kl}\overline{S}_l = \Omega_{\Delta lk}(\overline{S}_k - \overline{S}_l).\end{aligned} \tag{C.12}$$

By noting that the same derivation could alternatively have been carried out with $\mathbf{C}^{\mathrm{etr}}$ (with eigenvalues $\overline{\lambda}^2$) instead of $\overline{\mathbf{S}}$ and using

$$\mathbf{d}_\Delta = \mathrm{sym}(\Delta\mathbf{F}\mathbf{F}^{-1}), \quad \Delta\mathbf{C}^{\mathrm{etr}} = 2\mathbf{F}^{\mathrm{etr}\top}\mathbf{d}_\Delta\mathbf{F}^{\mathrm{etr}}, \tag{C.13}$$

one can reformulate (C.12) as follows

$$\begin{aligned}\Omega_{\Delta lk} &= \frac{1}{2(\overline{S}_k - \overline{S}_l)}(\overline{\mathbf{N}}_k \otimes \overline{\mathbf{N}}_l + \overline{\mathbf{N}}_l \otimes \overline{\mathbf{N}}_k) : \Delta\overline{\mathbf{S}} \\ &= \frac{1}{2(\overline{\lambda}_k^2 - \overline{\lambda}_l^2)}(\overline{\mathbf{N}}_k \otimes \overline{\mathbf{N}}_l + \overline{\mathbf{N}}_l \otimes \overline{\mathbf{N}}_k) : \Delta\mathbf{C}^{\mathrm{etr}} \\ &= \frac{\overline{\lambda}_k\overline{\lambda}_l}{\overline{\lambda}_k^2 - \overline{\lambda}_l^2}(\mathbf{n}_k \otimes \mathbf{n}_l + \mathbf{n}_l \otimes \mathbf{n}_k) : \mathbf{d}_\Delta.\end{aligned} \tag{C.14}$$

With

$$\text{(C.15)}\qquad \mathbf{F}^{\mathrm{etr}}\overline{S}_i(\Delta\mathbf{N}_i\otimes\mathbf{N}_i+\mathbf{N}_i\otimes\Delta\mathbf{N}_i)\mathbf{F}^{\mathrm{etr}\top} = \sum_{\substack{j=1\\ j\neq i}}^{3}\frac{\tau_i}{\overline{\lambda}_i^2}\overline{\lambda}_j\overline{\lambda}_i(\mathbf{n}_j\otimes\mathbf{n}_i+\mathbf{n}_i\otimes\mathbf{n}_j)\otimes(\mathbf{n}_i\otimes\mathbf{n}_j+\mathbf{n}_j\otimes\mathbf{n}_i):\mathbf{d}_\Delta\frac{\overline{\lambda}_i\overline{\lambda}_j}{\overline{\lambda}_i^2-\overline{\lambda}_j^2},$$

where the τ_i are the eigenvalues of $\boldsymbol{\tau}$, and

$$\text{(C.16)}\qquad \Delta(\overline{\lambda}_i^2)=\overline{\mathbf{N}}_i\otimes\overline{\mathbf{N}}_i:\Delta\mathbf{C}^{\mathrm{etr}}=2\overline{\lambda}_i^2\mathbf{n}_i\otimes\mathbf{n}_i:\mathbf{d}_\Delta$$

$$\text{(C.17)}\qquad \Delta\left(\frac{1}{\overline{\lambda}_i^2}\right)=-\frac{2}{\overline{\lambda}_i^4}\,\overline{\lambda}_i^2\mathbf{n}_i\otimes\mathbf{n}_i:\mathbf{d}_\Delta$$

one obtains

(C.18)

$$\mathbf{F}^{\mathrm{etr}}\Delta\overline{\mathbf{S}}\mathbf{F}^{\mathrm{etr}\top}=\sum_{i=1}^{3}\Delta\left(\frac{\tau_i}{\overline{\lambda}_i^2}\right)\overline{\lambda}_i^2\mathbf{n}_i\otimes\mathbf{n}_i\otimes\mathbf{n}_i\otimes\mathbf{n}_i:\mathbf{d}_\Delta + \sum_{\substack{j=1\\ j\neq i}}^{3}\frac{\tau_i\overline{\lambda}_j^2}{\overline{\lambda}_i^2-\overline{\lambda}_j^2}(\mathbf{n}_i\otimes\mathbf{n}_j+\mathbf{n}_j\otimes\mathbf{n}_i)\otimes(\mathbf{n}_i\otimes\mathbf{n}_j+\mathbf{n}_j\otimes\mathbf{n}_i):\mathbf{d}_\Delta.$$

Using the eigensystem of τ, one can further show that $\Delta\tau_i=\sum_j\partial\tau_i/\partial\varepsilon_j d_{\Delta j}$. Thus, the algorithmic tangent $\hat{\underline{c}}^{\mathrm{ar}}$ expressed in the Mandel notation with respect to the eigensystem of $\boldsymbol{\tau}$ is given by

$$\text{(C.19)}\qquad \hat{\underline{c}}^{\mathrm{ar}}=\begin{pmatrix}\tilde{c}^{\mathrm{a}}_{11}-2\tau_1 & \tilde{c}^{\mathrm{a}}_{12} & \tilde{c}^{\mathrm{a}}_{13} & 0 & 0 & 0\\ \tilde{c}^{\mathrm{a}}_{21} & \tilde{c}^{\mathrm{a}}_{22}-2\tau_2 & \tilde{c}^{\mathrm{a}}_{23} & 0 & 0 & 0\\ \tilde{c}^{\mathrm{a}}_{31} & \tilde{c}^{\mathrm{a}}_{32} & \tilde{c}^{\mathrm{a}}_{33}-2\tau_3 & 0 & 0 & 0\\ 0 & 0 & 0 & \hat{c}^{\mathrm{ar}}_{44} & 0 & 0\\ 0 & 0 & 0 & 0 & \hat{c}^{\mathrm{ar}}_{55} & 0\\ 0 & 0 & 0 & 0 & 0 & \hat{c}^{\mathrm{ar}}_{66}\end{pmatrix}$$

with

$$\text{(C.20)}\qquad \hat{c}^{\mathrm{ar}}_{(3+i)(3+i)}=2\frac{\tau_{p(i,1)}\overline{\lambda}^2_{p(i,2)}-\tau_{p(i,2)}\overline{\lambda}^2_{p(i,1)}}{\overline{\lambda}^2_{p(i,1)}-\overline{\lambda}^2_{p(i,2)}},\qquad p=\begin{pmatrix}2&3\\1&3\\1&2\end{pmatrix}.$$

Introducing the following notation

$$\text{(C.21)}\qquad \mathbf{n}_i=\mathbf{Q}\mathbf{e}_i=\sum_{j=1}^{3}Q_{ji}\mathbf{e}_i,\qquad \mathbf{Q}=\sum_{i=1}^{3}\mathbf{n}_i\otimes\mathbf{e}_i,$$

the algorithmic tangent $\mathbf{c}^{\mathrm{a}}$ can be written as

$$\begin{aligned}\mathbf{c}^{\mathrm{a}} &= c^{\mathrm{ar}}_{ijkl}\mathbf{n}_i \otimes \mathbf{n}_j \otimes \mathbf{n}_k \otimes \mathbf{n}_l \\ &= Q_{Ii} \otimes Q_{Jj} \otimes Q_{Kk} \otimes Q_{Ll}\ c^{\mathrm{ar}}_{ijkl}\ \mathbf{n}_i \otimes \mathbf{n}_j \otimes \mathbf{n}_k \otimes \mathbf{n}_l.\end{aligned} \tag{C.22}$$

Finally, the algorithmic tangent in matrix notation $\hat{\underline{c}}^{\mathrm{a}}$ reads

$$\hat{\underline{c}}^{\mathrm{a}} = (\underline{Q} \overset{s}{\square} \underline{Q}^{\top})\ \hat{\underline{c}}^{\mathrm{ar}}\ (\underline{Q}^{\top} \overset{s}{\square} \underline{Q}), \tag{C.23}$$

where the symmetric box product (a 6×6-matrix) is defined through

$$(\underline{A} \overset{s}{\square} \underline{A}^{\top})\underline{C} = \underline{A}\,\mathrm{sym}(\underline{\mathrm{C}})\underline{\mathrm{A}}^{\top}.$$

Acknowledgements

This work was supported by the German Federal Ministry of Economic Affairs and Energy under the grant 03ET7078E (project "Innovationen zur Entwicklung von Turbogeneratoren zur Unterstützung der Energiewende (FlexGen)").

Supported by:

Federal Ministry for Economic Affairs and Energy

on the basis of a decision by the German Bundestag

The financial support is gratefully acknowledged by the authors.

References

1. B.D. COLEMAN, M.E. GURTIN, *Thermodynamics with internal state variables*, The Journal of Chemical Physics, **47**, 2, 597–613, 1967.
2. E. Kröner, *Kontinuumstheorie der Versetzungen und Eigenspannungen*, Springer, Berlin, 1958.
3. E.H. LEE, *Elastic-plastic deformation at finite strains*, Journal of Applied Mechanics, ASME, **36**, 1, 1–6, 1969.
4. A. Lion, *Constitutive modelling in finite thermoviscoplasticity: a physical approach based on nonlinear rheological models*, International Journal of Plasticity, **16**, 5, 469–494, 2000.

5. W. DETTMER, S. REESE, *On the theoretical and numerical modelling of Armstrong–Frederick kinematic hardening in the finite strain regime*, Computer Methods in Applied Mechanics and Engineering, **193**, 1-2, 87–116, 2004.

6. G. WEBER, L. ANAND, *Finite deformation constitutive equations and a time integration procedure for isotropic, hyperelastic-viscoplastic solids*, Computer Methods in Applied Mechanics and Engineering, **79**, 2, 173–202, 1990.

7. A.L. ETEROVIC, J.-K. BATHE, *A hyperelastic-based large strain elasto-plastic constitutive formulation with combined isotropic-kinematic hardening using the logarithmic stress and strain measures*, International Journal for Numerical Methods in Engineering, **30**, 6, 1099–1114, 1990.

8. J.C. SIMO, *Algorithms for static and dynamic multiplicative plasticity that preserve the classical return mapping schemes of the infinitesimal theory*, Computer Methods in Applied Mechanics and Engineering, **99**, 1, 61–112, 1992.

9. B. HALPHEN, Q. NGUYEN, *Generalized standard materials*, Journal de Mécanique, **14**, 1, 39–63, 1975.

10. M.A. Biot, *Mechanics of Incremental Deformations*, Wiley, New York, 1965.

11. P.P. CASTANEDA, P. SUQUET, *Nonlinear composites*, [in:] Advances in Applied Mechanics, **34**, pp. 171–302, Elsevier, 1997.

12. M. ORTIZ, L. STAINIER, *The variational formulation of viscoplastic constitutive updates*, Computer Methods in Applied Mechanics and Engineering, **171**, 3-4, 419–444, 1999.

13. A. MIELKE, *Evolution of rate-independent systems*, Evolutionary Equations, **2**, 461–559, 2005.

14. M. ORTIZ, E. REPETTO, *Nonconvex energy minimization and dislocation structures in ductile single crystals*, Journal of the Mechanics and Physics of Solids, **47**, 2, 397–462, 1999.

15. C. CARSTENSEN, K. HACKL, A. MIELKE, *Non-convex potentials and microstructures in finite-strain plasticity*, Proceedings of the Royal Society A, **458**, 2018, 299–317, 2002.

16. L. KACHANOV, *Time of the rupture process under creep conditions*, Issue of the Academy of Sciences of the USSR Department of Technical Sciences, **8**, 26–31, 1958.

17. D. HAYHURST, F. LECKIE, *The effect of creep constitutive and damage relationships upon the rupture time of a solid circular torsion bar*, Journal of the Mechanics and Physics of Solids, **21**, 6, 431–432, 1973.

18. J. LEMAITRE, *Coupled elasto-plasticity and damage constitutive equations*, Computer Methods in Applied Mechanics and Engineering, **51**, 1, 31–49, 1985.

19. T. BREPOLS, S. WULFINGHOFF, S. REESE, *Gradient-extended two-surface damage-plasticity: micromorphic formulation and numerical aspects*, International Journal of Plasticity, **97**, 64–106, 2017.

20. D. KRAJCINOVIC, G. FONSEKA, *The continuous damage theory of brittle materials, part 1: general theory*, Journal of Applied Mechanics, **48**, 4, 809–815, 1981.

21. J. LEMAITRE, R. DESMORAT, M. SAUZAY, *Anisotropic damage law of evolution*, European Journal of Mechanics-A/Solids, **19**, 2, 187–208, 2000.

22. M. Fassin, R. Eggersmann, S. Stephan, S. Reese, *Efficient algorithmic incorporation of tension compression asymmetry into an anisotropic damage model*, Computer Methods in Applied Mechanics and Engineering, **354**, 932–962, 2019.

23. J.-L. Chaboche, *Damage induced anisotropy: on the difficulties associated with the active/passive unilateral condition*, International Journal of Damage Mechanics, **1**, 2, 148–171, 1992.

24. S. Wulfinghoff, M. Fassin, S. Reese, *A damage growth criterion for anisotropic damage models motivated from micromechanics*, International Journal of Solids and Structures, **121**, 21–32, 2017

25. Z. P. Bazant, G. Pijaudier-Cabot, *Nonlocal continuum damage, localization instability and convergence*, Journal of Applied Mechanics, **55**, 2, 287–293, 1988.

26. R. Peerlings, W. Brekelmans, J. De Vree, *Gradient enhanced damage for quasi-brittle materials*, International Journal for Numerical Methods in Engineering, **39**, 3391–3403, 1996.

27. E. Fried, M.E. Gurtin, *Continuum theory of thermally induced phase transitions based on an order parameter*, Physica D: Nonlinear Phenomena, **68**, 3-4, 326–343, 1993.

28. M.E. Gurtin, *Generalized Ginzburg–Landau and Cahn–Hilliard equations based on a microforce balance*, Physica D: Nonlinear Phenomena, **92**, 3-4, 178–192, 1996.

29. M.E. Gurtin, *On the plasticity of single crystals: free energy, microforces, plastic-strain gradients*, Journal of the Mechanics and Physics of Solids, **48**, 5, 989–1036, 2000.

30. S. Wulfinghoff, T. Böhlke, *Equivalent plastic strain gradient enhancement of single crystal plasticity: theory and numerics*, Proceedings of the Royal Society A, **468**, 2682–2703, 2012.

31. M. Ziemann, Y. Chen, O. Kraft, E. Bayerschen, S. Wulfinghoff, C. Kirchlechner, N. Tamura, T. Böhlke, M. Walter, P. Gruber, *Deformation patterns in cross-sections of twisted bamboo-structured Au microwires*, Acta Materialia, **97**, 216–222, 2015.

32. A. Alipour, S. Reese, B. Svendsen, S. Wulfinghoff, *A grain boundary model considering the grain misorientation within a geometrically nonlinear gradient-extended crystal viscoplasticity theory*, Proceedings of the Royal Society A, **476**, 2235, 20190581, 2020.

33. B. Bourdin, G.A. Francfort, J.-J. Marigo, *The variational approach to fracture*, Journal of Elasticity, **91**, 1-3, 5–148, 2008.

34. B. Bourdin, G.A. Francfort, J.-J. Marigo, *Numerical experiments in revisited brittle fracture*, Journal of the Mechanics and Physics of Solids, **48**, 4, 797–826, 2000.

35. C. Kuhn, R. Müller, *A continuum phase field model for fracture*, Engineering Fracture Mechanics, **77**, 18, 3625–3634, 2010.

36. C. Miehe, M. Hofacker, F. Welschinger, *A phase field model for rate-independent crack propagation: robust algorithmic implementation based on operator splits*, Computer Methods in Applied Mechanics and Engineering, **199**, 45, 2765–2778, 2010.

37. C. Miehe, F. Welschinger, M. Hofacker, *Thermodynamically consistent phase-field models of fracture: variational principles and multi-field FE implementations*, International Journal for Numerical Methods in Engineering, **83**, 10, 1273–1311, 2010.

38. G.A. FRANCFORT, J.-J. MARIGO, *Revisiting brittle fracture as an energy minimization problem*, Journal of the Mechanics and Physics of Solids, **46**, 8, 1319–1342, 1998.

39. R. ALESSI, J.-J. MARIGO, S. VIDOLI, *Gradient damage models coupled with plasticity: variational formulation and main properties*, Mechanics of Materials, **80**, 351–367, 2015.

40. C. KUHN, T. NOLL, R. MÜLLER, *On phase field modeling of ductile fracture*, GAMM-Mitteilungen, **39**, 1, 35–54, 2016.

41. C. MIEHE, F. ALDAKHEEL, A. RAINA, *Phase field modeling of ductile fracture at finite strains: a variational gradient-extended plasticity-damage theory*, International Journal of Plasticity, **84**, 1–32, 2016.

42. C. MIEHE, *A multi-field incremental variational framework for gradient-extended standard dissipative solids*, Journal of the Mechanics and Physics of Solids, **59**, 898–923, 2011.

43. W. HAN, B.D. REDDY, *Plasticity: Mathematical Theory and Numerical Analysis*, Springer, 1999.

44. J. LEMAITRE, *How to use damage mechanics*, Nuclear Engineering and Design, **80**, 2, 233–245, 1984.

45. S. FOREST, *Micromorphic approach for gradient elasticity, viscoplasticity, and damage*, Journal of Engineering Mechanics, **135**, 117–131, 2009.

46. R.B. SEYMOUR, *Origin and early development of rubber-toughened plastics*, [in:] Rubber-Toughened Plastics, chapter 1, 3–13, 1989.

47. A.C. GARG, Y.-W. MAI, *Failure mechanisms in toughened epoxy resins – a review*, Composites Science and Technology, **31**, 3, 179–223, 1988.

48. L.T. MANZIONE, J.K. GILLHAM, C.A. MCPHERSON, *Rubber-modified epoxies. I. Transitions and morphology*, Journal of Applied Polymer Science, **26**, 3, 889–905, 1981.

49. R. BAGHERI, B.T. MAROUF, R.A. PEARSON, *Rubber-toughened epoxies: a critical review*, Polymer Reviews, **49**, 3, 201–225, 2009.

50. A.F. YEE, R.A. PEARSON, *Toughening mechanisms in elastomer-modified epoxies. Part 1: Mechanical studies*, Journal of Materials Science, **21**, 2462–2474, 1986.

51. Y. HUANG, A.J. KINLOCH, *Modelling of the toughening mechanism in rubber-modified epoxy polymers*, Journal of Materials Science, **27**, 2763–2769, 1992.

52. G. GIANNAKOPOULOS, K. MASANIA, A.C. TAYLOR, *Toughening of epoxy using core-shell particles*, Journal of Materials Science, **46**, 327–338, 2011.

53. E. VAN DER GIESSEN, T. SEELIG, *Computational modeling of rubber-toughening in amorphous thermoplastic polymers: a review*, International Journal of Fracture, **196**, 1-2, 207–222, 2015.

54. D. KOBLAR, J. ŠKOFIC, M. BOLTEŽAR, *Evaluation of the Young's modulus of rubber-like materials bonded to rigid surfaces with respect to Poisson's ratio*, Strojniški vestnik – Journal of Mechanical Engineering, **60**, 7-8, 506–511, 2014.

55. R. SMIT, W. BREKELMANS, H. MEIJER, *Prediction of the large-strain mechanical response of heterogeneous polymer systems: local and global deformation behaviour of a representative volume element of voided polycarbonate*, Journal of the Mechanics and Physics of Solids, **47**, 2, 201–221, 1999.

56. *On cavitation, post-cavitation and yield in amorphous polymer-rubber blends*, Journal of the Mechanics and Physics of Solids, **47**, 4, 843–876, 1999.

57. K. Pijnenburg, E. Van der Giessen, *Macroscopic yield in cavitated polymer blends*, International Journal of Solids and Structures, **38**, 20, 3575–3598, 2001.

58. H.E.H. Meijer, L.E. Govaert, *Multi-scale analysis of mechanical properties of amorphous polymer systems*, Macromolecular Chemistry and Physics, **204**, 2, 274–288, 2003.

59. D.K. Rajak, D.D. Pagar, P.L. Menezes, E. Linul, *Fiber-reinforced polymer composites: manufacturing, properties, and applications*, Polymers, **11**, 10, 2019.

60. G. Gao, Y. Li, *Mechanical properties of woven glass-fiber reinforced polymer composites*, Emerging Materials Research, **5**, 2016.

61. R.L. Taylor, *FEAP – Finite Element Analysis Program*, http://www.ce.berkeley/feap, 2014.

62. D. Quan, A. Ivankovic, *Effect of core–shell rubber (CSR) nano-particles on mechanical properties and fracture toughness of an epoxy polymer*, Polymer, **66**, 16–28, 2015.

63. B.A. Bednarcyk, B. Stier, J.-W. Simon, S. Reese, E.J. Pineda, *Meso-and micro-scale modeling of damage in plain weave composites*, Composite Structures, **121**, 258–270, 2015.

64. A. Melro, P. Camanho, F.A. Pires, S. Pinho, *Numerical simulation of the non-linear deformation of 5-harness satin weaves*, Computational Materials Science, **61**, 116–126, 2012.

65. N. Naik, P. Shembeka, *Elastic behavior of woven fabric composites: I—lamina analysis*, **12**, 2196–2225, 1992.

66. S. Géhant, C. Fond, R. Schirrer, *Criteria for cavitation of rubber particles: influence of plastic yielding in the matrix*, International Journal of Fracture, **122**, 3, 161–175, 2003.

67. F. Guild, A. Kinloch, A. Taylor, *Particle cavitation in rubber toughened epoxies: the role of particle size*, Journal of Materials Science, **45**, 14, 3882–3894, 2010.

68. G. Jacob, J. Starbuck, J. Fellers, S. Simunovic, *Effect of fiber volume fraction, fiber length and fiber tow size on the energy absorption of chopped carbon fiber-polymer composites*, Polymer Composites, **26**, 293–305, 2005.

69. E. Totry, J.M. Molina-Aldareguía, C. González, J. LLorca, *Effect of fiber, matrix and interface properties on the in-plane shear deformation of carbon-fiber reinforced composites*, Composites Science and Technology, **70**, 6, 970–980, 2010.

70. S. Yoon, N. Takano, Y. Korai, *Some influential factors for crack formation*, Journal of Materials Science, **32**, 3, 1987.

71. M. Mehdikhani, L. Gorbatikh, I. Verpoest, S. Lomov, *Voids in fiber-reinforced polymer composites: a review on their formation, characteristics, and effects on mechanical performance*, Journal of Composite Materials, **53**, 002199831877215, 2018.

Received May 20, 2021; revised version August 14, 2021.
Published online October 20, 2021.